NOTCH1 mediates a switch between two distinct secretomes during senescence

Hoare, Matthew; Ito, Yoko; Kang, Tae-Won; Weekes, Michael P; Matheson, Nicholas J; Patten, Daniel; Shetty, Shishir; Parry, Aled J; Menon, Suraj; Salama, Rafik; Antrobus, Robin; Tomimatsu, Kosuke; Howat, William; Lehner, Paul J; Zender, Lars; Narita, Masashi

DOI:
10.1038/ncb3397

NOTCH1 mediates a switch between two distinct secretomes during senescence

Matthew Hoare[1,2], Yoko Ito[1], Tae-Won Kang[3], Michael P. Weekes[2,4], Nicholas J. Matheson[2,4], Daniel A. Patten[5], Shishir Shetty[5], Aled J. Parry[1], Suraj Menon[1], Rafik Salama[1], Robin Antrobus[4], Kosuke Tomimatsu[1], William Howat[1], Paul J. Lehner[2,4], Lars Zender[3] and Masashi Narita[1,*]

[1]University of Cambridge, Cancer Research UK Cambridge Institute, Robinson Way, Cambridge, CB2 0RE, UK.

[2]University of Cambridge, Department of Medicine, Addenbrooke's Hospital, Cambridge, CB2 0QQ, UK.

[3]Division of Translational Gastrointestinal Oncology, Dept. of Internal Medicine I, University Hospital Tuebingen, Otfried-Mueller-Strasse 12, 72076 Tuebingen, Germany & Translational Gastrointestinal Oncology Group within the German Consortium for Translational Cancer Research (DKTK), German Cancer Research Center (DKFZ), Heidelberg, Germany.

[4]University of Cambridge, Cambridge Institute for Medical Research, Addenbrooke's Hospital, Cambridge, CB2 0XY, UK.

[5]National Institute of Health Research (NIHR) Birmingham Liver Biomedical Research Unit (BRU), Centre for Liver Research, University of Birmingham, Birmingham, B15 2TT, UK.

*Correspondence: masashi.narita@cruk.cam.ac.uk

ABSTRACT

Senescence, a persistent form of cell cycle arrest, is often associated with a diverse secretome, which provides complex functionality for senescent cells within the tissue microenvironment. We show that oncogene-induced senescence (OIS) is accompanied by a dynamic fluctuation of NOTCH1 activity, which drives a TGF-β-rich secretome, whilst suppressing the senescence-associated pro-inflammatory secretome through inhibition of C/EBPβ. NOTCH1 and NOTCH1-driven TGF-β contribute to 'lateral induction of senescence' through a juxtacrine NOTCH-JAG1 pathway. In addition, NOTCH1 inhibition during senescence facilitates upregulation of pro-inflammatory cytokines, promoting lymphocyte recruitment and senescence surveillance in vivo. Because enforced activation of NOTCH1 signalling confers a near mutually exclusive secretory profile compared to typical senescence, our data collectively indicate that the dynamic alteration of NOTCH1 activity during senescence dictates a functional balance between these two distinct secretomes: one representing TGF-β and the other pro-inflammatory cytokines, highlighting that NOTCH1 is a temporospatial controller of secretome composition.

INTRODUCTION

Cellular senescence is an autonomous tumour suppressor mechanism, whereby various triggers drive a stable proliferative arrest. Senescence is accompanied by diverse biochemical changes including upregulation of CDK inhibitors, the accumulation of senescence-associated β-galactosidase (SA-β-gal) activity, and expression of a wide variety of secretory proteins[1,2]. These features of senescence have been recapitulated by in vivo models, including both pathological and physiological contexts[3].

Senescent cells have profound non-autonomous functionality in the tissue microenvironment through the senescence-associated secretory phenotype (SASP)[2]. Previous studies have demonstrated heterogeneous effects of the SASP upon tumorigenesis. The SASP can reinforce the senescent phenotype in both an autocrine and paracrine fashion[4-6] and activate immune clearance of senescent cells[7-9] from tissues, thereby contributing to tumour suppression. Some tumorigenic activities of SASP have also been shown through promoting cellular growth and epithelial–mesenchymal transition in neighbouring immortalised or transformed epithelial cells[10,11]. In addition, SASP components, among others, include inflammatory cytokines and matrix-modifying enzymes, which play key roles in the clearance of senescent or damaged cells and resolution of tissue injury, respectively. Thus, it is conceivable that both the relative and absolute expression of SASP components is dynamic and under tight regulation. However, the basis for the regulation of different SASP components or controlling the net function of the SASP is unclear.

NOTCH signalling is evolutionarily conserved and involved in a wide range of developmental and physiological processes, controlling cell-fate specification and stem cell homeostasis[12] In addition, alterations of the NOTCH pathway have been linked to stress response and tumorigenesis, where it can be oncogenic or tumour suppressive depending on tissue and context[13]. There are four NOTCH receptors, which bind the Jagged (JAG) and Delta-like family of ligands[12]. Upon ligand binding the NOTCH receptors undergo a series of proteolytic cleavage events liberating the intracellular domain (ICD), which subsequently translocates to the nucleus to bind a multi-molecular complex, including both the DNA-binding protein, RBP-J and Mastermind-like (MAML) co-activators[12] and drive transcription of NOTCH-target genes, such as the HES/HEY family of transcription factors (TFs). Importantly, NOTCH ligands are also transmembrane proteins; thus, signalling is thought to be restricted to adjacent cells through juxtacrine interaction, and the role of NOTCH in autocrine or paracrine signalling through secreted factors remains unclear.

Through a quantitative cell surface proteome of oncogene-induced senescent (OIS) cells and subsequent validation, we have identified a global upregulation of NOTCH1 that is accompanied by dynamic alteration of its downstream activity during senescence. We describe how NOTCH1 functions as a master regulator of SASP composition through a temporal and functional switch between two distinct secretomes, representing TGF-β or pro-inflammatory cytokines, in part through downregulation of C/EBPβ. We show that inhibiting Notch signalling promotes clearance of OIS cells in the liver,

implying a unique therapeutic opportunity to target senescent cells through modulation of immune surveillance.

RESULTS

Plasma membrane proteome in OIS

To gain a better understanding of the phenotype of OIS cells, particularly potential mediators of non-cell-autonomous signalling, we conducted a proteomic screen of plasma membrane (PM) surface proteins utilising a quantitative SILAC approach[14] in IMR90 human diploid fibroblasts (HDFs) expressing oncogenic $HRAS^{G12V}$ in a 4-hydroxytamoxifen (4OHT)-inducible form (ER:$HRAS^{G12V}$) (Fig. 1a, Supplementary Fig. 1A)[15]. We identified peptides from 1502 independent proteins with. enrichment for localisation in PM or extracellular compartments in Gene Ontology (GO) analysis (Fig. 1b). Of the 1502 proteins, 521 were identified with 'high confidence' (see METHODS) with 32 and 135 significantly up and downregulated respectively in $HRAS^{G12V}$-induced senescent (RIS) cells (Fig. 1c, Supplementary Table 1).

To validate our proteomic findings, we compared the RIS-associated PM changes with transcriptomic data and identified a significant positive correlation between mRNA and protein changes during RIS (Supplementary Fig. 1B).

NOTCH1 is upregulated in OIS

To understand signalling networks involving senescence-associated PM proteins we conducted network enrichment analysis, utilising both

transcriptomic and proteomic data. The highest enriched network contained the NOTCH1 receptor as a major network hub and its canonical targets (HES1, HEY1, and HEYL) and binding partners (RBPJ and MAML3) (Fig. 1c, Supplementary Fig. 1C).

Utilising flow cytometry we confirmed the substantial upregulation of cell surface NOTCH1 during senescence induced by different triggers (oncogenic MEK or DNA damage) or RIS in different HDFs (Fig. 1d, Supplementary Fig. 1D, E). In contrast, bypass of RIS through co-expression of the adenoviral oncoprotein, E1A failed to up-regulate cell surface NOTCH1 on IMR90 cells (Fig. 1d). Although the NOTCH pathway has recently been implicated in senescence[16-18], its functional relevance is unclear.

NOTCH1 signalling is dynamically regulated during senescence

We next investigated the temporal changes of cell surface NOTCH1 and its downstream activity after ER:HRAS^{G12V} induction. In this system, senescence develops progressively from an initial mitotic phase (~d1) to senescence establishment (~d6) (Supplementary Fig. 1A)[15]. After a slight reduction at the mitotic phase, cell surface NOTCH1 continually increased during RIS (Fig. 2a). However, the cleaved, active NOTCH1 intracellular domain (N1ICD) and the canonical NOTCH1-target HES1 were transiently upregulated during the transition to senescence, but returned to near basal level at full senescence (Fig. 2b). The transient activation of NOTCH1 signalling, despite increased cell surface NOTCH1, was also observed during DNA damage-induced senescence (DDIS) (Fig. 2c, Fig. 1d right)[19].

Characterised SASP components include multiple pro-inflammatory cytokines, such as IL-1, IL-6 and IL-8[6,11,20,21]. More recently, TGF-β ligands have been identified as SASP components, which are involved in senescence induction, in part through inducing p15 and p21[4,5]. IL-6 and IL-8 were primarily upregulated at full senescence. However, we found a transient induction of TGF-β ligands during both RIS and DDIS, reminiscent of the N1ICD expression pattern (Fig. 2b, c, Supplementary Fig. 2A), suggesting that NOTCH signalling temporally correlates with the reciprocal induction of TGF-β and pro-inflammatory cytokines during senescence.

NOTCH1 reciprocally regulates TGF-β and pro-inflammatory cytokines

To examine the relationship between NOTCH1 and regulation of secretory factors during RIS, we first introduced a dominant negative form of MAML1, fused to mVenus (dnMAML1-mVenus), into ER:RAS^{G12V}-expressing IMR90 cells. At d3 after ER:RAS^{G12V} induction, expression of dnMAML1 led to minimal effect upon proliferation, but completely blocked the induction of HES1 (Fig. 2d). This inhibition of NOTCH signalling significantly reduced the upregulation of *TGFB1*, suggesting that NOTCH is upstream of HRAS^{G12V}-driven TGF-β induction (Fig. 2d). Conversely, upregulation of pro-inflammatory cytokines (IL-8, *IL1A*, and *IL1B*) was enhanced by dnMAML1, suggesting that activated NOTCH1, during senescence transition, negatively regulates the expression of pro-inflammatory cytokines. Similar results were obtained pharmacologically with DAPT, a gamma secretase inhibitor, which blocks cleavage and release of the N1ICD (Supplementary Fig. 2B). Notably,

the endogenous levels of N1ICD were modestly increased in the presence of dnMAML1 regardless of $HRAS^{G12V}$-induction (Figure 2d). This is consistent with previous studies showing that N1ICD levels are controlled by negative feedback through MAML-dependent proteasomal degradation, providing a potential mechanism for the decoupling of surface NOTCH1 and N1ICD levels [22].

We next introduced a doxycycline-inducible N1ICD-FLAG system into IMR90 cells (Supplementary Fig. 2C). Restoration of N1ICD at the late phase of RIS (d6) led to a dose-dependent decrease in *IL1A*, *IL1B* and IL-8 expression and a dose-dependent increase in *TGFB1* expression, with minimal impact on senescence arrest (Fig. 2e). Therefore, during RIS, the dynamic alteration of NOTCH1 controls the temporally reciprocal pattern of TGF-β1 and pro-inflammatory cytokines and manipulating NOTCH signalling allows for SASP modulation with senescence arrest being maintained.

Enforced activation of NOTCH1 induces a unique senescence phenotype in HDFs

Consistent with recent reports[16-18], expression of ectopic N1ICD drove a senescence-like morphological change with stable cell cycle arrest, although accumulation of SA-β-gal activity was relatively modest (Fig. 3a, b, Supplementary Fig. 2D, E). Note, proliferative arrest was maintained even after removal of ectopic N1ICD, the hallmark of senescence (Supplementary Fig. 2E). Overexpression of N1ICD was sufficient for reduction of basal IL-8 levels as well as induction of TGF-β1 and its downstream effector

phosphorylated SMAD3 (Fig. 3a, c, d). Thus, ectopic N1ICD induces senescence that is distinct from RIS or DDIS, particularly in its SASP composition.

To understand the broader implications of NOTCH1 in the control of secretome composition, we performed mRNA-seq analysis of senescent IMR90 cells driven by $HRAS^{G12V}$, DNA damage, or N1ICD. Transcriptional profiling of secretory factors of RIS and DDIS shared large clusters (Fig. 3e). Gene Set Enrichment Analysis (GSEA) showed that all types of senescence shared a common cell-cycle signature (Supplementary Fig. 3A). However, the secretome expression profile of N1ICD-induced senescence (NIS) exhibited an almost mutually exclusive pattern with RIS and DDIS, particularly in those shared clusters (Fig. 3e). Many secretory factors that have been associated with RIS or DDIS, such as pro-inflammatory cytokines and matrix metalloproteinases (*MMP1/3/10*), were repressed by ectopic N1ICD. Downregulated secretory factors at d6 of RIS, including TGF-β ligands (*TGFB1/2/3*) were upregulated by ectopic N1ICD in IMR90 cells. GSEA revealed a close association of TGF-β1 signatures with NIS (Supplementary Fig. 3B). To understand the relative dominance of RAS and N1ICD upon the secretome composition we analysed secretome transcriptional data from IMR90 cells undergoing RIS, NIS or expressing both RAS and N1ICD (N+RIS). Unsupervised clustering revealed the similarity between NIS and N+RIS secretomes, where ectopic N1ICD mostly overcame the RIS pattern (Supplementary Fig. 3C). Interestingly, such dominance of NOTCH over RAS also applied to *GLB1*, encoding the lysosomal enzyme responsible for SA-β-

Gal activity[23], potentially explaining the modest SA-β-Gal activity of NIS (Fig. 3b). Altogether, our data suggest that NIS and RIS are associated with reciprocal secretory profiles, and that dynamic NOTCH1 activity during senescence determines the balance between two extremities: one representing TGF-β ligands and the other representing 'classical' SASP components including pro-inflammatory cytokines.

NOTCH1-driven cell-autonomous senescence is partly dependent on TGF-β signalling

To understand how N1ICD induces senescence, we expressed N1ICD in the presence or absence of inhibitors of the TGF-β receptor (TGFBR1). Inhibition of TGF-β signalling prevented upregulation of TGF-β targets, *p15* and *TGFB-induced* (*TGFBI*), in N1ICD-expressing cells, and partly rescued the anti-proliferative effect of N1ICD (Fig. 3f, Supplementary Fig. 4A, left). Similar results were also obtained by expression of a dominant negative form of SMAD4 (dnSMAD4) (Supplementary Fig. 4B, left)[24]. Importantly, recombinant TGF-βs alone had no anti-proliferative effect on IMR90 cells (Supplementary Fig. 4C and D), suggesting that NOTCH-driven TGF-β signalling contributes to senescence cooperatively with other NOTCH1-downstream factor(s), as yet to be elucidated.

Non-cell-autonomous effects of NOTCH1 on normal cells

To investigate the non-cell-autonomous effects of differing forms of senescence, we set up co-culture experiments of mRFP-labelled, otherwise normal, IMR90 cells with senescent IMR90 cells induced by N1ICD,

HRAS^{G12V} or DNA damage. To avoid confounding effects of the 'TGF-β phase' of SASP during RIS and DDIS, senescence was pre-induced for 4 days before co-culture. We found that mRFP-labelled cells co-cultured with NIS, but not late phase RIS or DDIS cells, at least in IMR90 cells, underwent a growth arrest, suggesting a key role for the NOTCH1-driven secretome in the transmission of senescence (Fig. 4a).

To understand signalling pathways that might underpin N1ICD-mediated non-autonomous growth arrest, we co-cultured NIS and mRFP-IMR90 cells for 72 hours prior to flow sorting and then analysing gene expression in both cell populations. Consistent with N1ICD-mediated induction of TGF-β ligands in the mono-culture experiments (Fig. 3c-e), both N1ICD-expressing and mRFP-cells exhibited upregulation of the TGF-β targets, *p15/CDKN2B* and *TGFBI* (Fig. 4b). Similarly to autonomous NOTCH1 activation, TGFBR1 inhibitors or dnSMAD4 partially rescued the non-autonomous growth arrest in mRFP-cells when co-cultured with N1ICD-expressing cells (Fig. 4c, Supplementary Fig. 4A, B).

To further examine whether N1ICD-expressing cells induce senescence in neighbouring cells, we took advantage of the difference in the drug selection markers of retroviral vectors expressing either N1ICD (or control vector) or mRFP: after co-culturing N1ICD-expressing cells (hygromycin resistant) and mRFP-expressing cells (puromycin resistant), cells were incubated with puromycin for 2 days to remove N1ICD-expressing cells (Fig. 4d). After additional culture for 5 days, mRFP cells that had been co-cultured with

N1ICD-expressing cells, but not with vector-expressing cells, exhibited a senescent phenotype (Fig. 4d, e). Importantly, this phenotype was maintained even after the removal of the signal-sending cells, indicating that the N1ICD-expressing cells transmitted a senescent phenotype to the neighbouring cells.

N1ICD-induced 'lateral induction' of senescence

The role of NOTCH in biological patterning during development is attributed to processes termed 'lateral inhibition' and 'lateral induction'[25]: NOTCH-mediated downregulation of NOTCH ligands in the same cells will negatively regulate NOTCH signalling in neighbouring cells (lateral inhibition), whereas NOTCH-mediated upregulation of NOTCH ligands will positively regulate NOTCH activity in neighbouring cells (lateral induction)[26].

Interestingly, activation of downstream NOTCH signalling was observed not only in the N1ICD-expressing cells, but also in the co-cultured target cells with increased expression of HES1 (Fig. 4b). In addition, basal levels of *IL1A* were repressed in both cell populations (Fig. 4b), suggesting that NOTCH signalling was transmitted from N1ICD-expressing cells to neighbouring cells. Among the five canonical NOTCH ligands[12], we found a strong, unique upregulation of *JAG1* upon ectopic N1ICD expression (Fig. 5a, Supplementary Fig. 5A). Although shedding of extracellular domain of JAG1 has been reported, we did not detect this in conditioned media (CM) from NIS cells (Supplementary Fig. 5B)[27]. Induction of JAG1 was also observed during the transition to RIS with up and subsequent down-regulation mirroring the dynamic expression of N1ICD (Supplementary Fig. 2A). Induction of senescence with increased

JAG1 was confirmed in N1ICD-expressing hTERT-RPE1 cells (Supplementary Fig. 5C). These results suggest that N1ICD activation induces a cell-contact dependent growth arrest through a process similar to embryonic lateral induction. To further corroborate this, we examined how downstream inhibition of NOTCH signalling in the mRFP-expressing target cells affected non-cell-autonomous suppression of proliferation in the co-culture system. Consistent with our hypothesis, use of DAPT led to a dose-dependent inhibition of the non-cell-autonomous growth arrest of mRFP-expressing cells co-cultured with N1ICD-expressing cells (Fig. 5b, Supplementary Fig. 5D). As expected, it had no effect upon autonomous cell growth in cells expressing N1ICD, which acts downstream of gamma secretase activity (Fig. 5c). More specifically, dnMAML1-mediated inhibition of NOTCH signalling only in the mRFP-expressing target cells also led to resistance to the non-cell-autonomous growth arrest in the co-culture system (Fig. 5d).

We next inhibited NOTCH ligand activity in N1ICD-expressing cells. RNAi-mediated knockdown of JAG1 in the N1ICD-expressing IMR90 cells had no effect upon cell autonomous growth of these cells (Fig. 5e, f), but led to a dose-dependent inhibition of the non-cell-autonomous growth arrest in the co-cultured mRFP-expressing cells (Fig. 5g, Supplementary Fig. 5D). Culturing the N1ICD- and mRFP-expressing cells apart using a transwell chamber led to only a marginal decrease in proliferation of the mRFP-labelled cells (Fig. 5h), supporting the critical role for cell-cell contact in activation of NOTCH signalling and subsequent senescence induction in cells adjacent to N1ICD-

expressing cells. Similar NOTCH-mediated senescence transmission was also observed in mRFP-expressing IMR90 cells co-cultured with N1ICD-expressing RPE1 cells, where JAG1 was upregulated (Supplementary Fig. 5C, E). Although it is known that TGF-β signalling can induce JAG1 expression[28], neither TGFBR1 inhibitors or expression of dnSMAD4 affected the N1ICD-mediated upregulation of *JAG1* in HDFs (Fig. 5i), reinforcing that NOTCH is an upstream regulator of TGF-β. Together, these data indicate that N1ICD-expression leads to cell-autonomous upregulation of both JAG1 and TGF-β ligands; the former triggers lateral induction of NOTCH signalling, and together with TGF-β signalling, induces senescence in neighbouring cells (Supplementary Fig. 5F). Interestingly, the NOTCH-mediated transmission of senescence was blocked by co-existing RIS cells, which were expressing dnMAML1 to minimise the inhibitory effect of NOTCH on the 'RIS-secretome', highlighting the functional distinction between non-autonomous activities of the two phases of RIS. This might also be involved in the negative feedback of NOTCH activity observed in the late phase of RIS in culture (Supplementary Fig. 5G).

NOTCH1 activation during OIS in vivo

To test whether Notch signalling is involved in senescence in vivo, we first examined $Kras^{G12D}$-driven pancreatic intraepithelial neoplasia (PanIN) in *$Kras^{LSL\text{-}G12D}$; p48-cre* mice, previously demonstrated to show evidence of senescence[29]. It was shown that Hes1 is upregulated in $Kras^{G12D}$-driven mouse PanIN[30-32]. While most cells in adult wild-type pancreas exhibited low levels of Notch1 (Supplementary Fig. 6A), Notch1 was highly upregulated in

PanIN cells that were positive for the senescence marker, Dec1[29], although the nuclear staining of Notch1 appeared heterogeneous (Supplementary Fig. 6A). Notch1 was also upregulated in acinar to ductal metaplasia, a potential histological precursor for PanIN, previously linked to senescence[33] (Supplementary Fig. 6A).

Non-cell-autonomous effects of NOTCH1 on immune clearance of senescent cells

We also examined the level of Notch1 in a mouse liver OIS model, in which transposable elements containing oncogenic *NRAS*^{G12V} are stably transduced to hepatocytes through the hydrodynamic tail-vein injection (HDTV): it was shown that *NRAS*^{G12V}-driven senescent hepatocytes are often surrounded by immune cells, and progressively cleared by a CD4+ T-cell-dependent immune reaction[8]. We found that cellular levels of Notch1 were upregulated in hepatocytes expressing NRAS^{G12V}, but not in hepatocytes expressing the non-functional NRAS$^{G12V/D38A}$ (Fig. 6a).

To test whether Notch inhibition during NRAS^{G12V}-driven hepatocyte senescence would modulate immune-mediated clearance of these cells, we compared two cohorts of mice, injected with *NRAS*^{G12V} or *NRAS*^{G12V} combined with *dnMAML1*. Consistent with previous reports[8], we observed a time-dependent clearance of NRAS^{G12V}-induced senescent hepatocytes (Fig. 6b, c). In the presence of Notch inhibition, this clearance was accelerated with a reduction in NRAS^{G12V}- and p21-expressing hepatocytes at d12 post-HDTV (Fig. 6b, c). Strikingly, in NRAS^{G12V}-expressing hepatocytes, the frequency of

nuclear Hes1 positive cells progressively increased over time (Fig. 6d, Supplementary Fig. 6B), while, at d12 when most $NRAS^{G12V}$-expressing hepatocytes had been eliminated, the frequency was more variable between mice. Thus, the dynamic regulation of Notch activity observed in vitro OIS/DDIS (Fig. 2b, c) was recapitulated in vivo. Moreover, NRAS-expressing hepatocytes were often associated with neighbouring Hes1- or p21-expressing hepatocytes that did not express NRAS, at least at d9 (Fig. 6d, Supplementary Fig. 6C, D), providing in vivo evidence for senescence-associated lateral induction of Notch signalling. Note, we failed to observe any inhibition of $NRAS^{G12V}$-driven senescence (probed by p21) by dnMAML1, particularly up to d9, in both NRAS-positive and negative hepatocytes (Fig. 6c, Supplementary Fig. 6E): we speculate that dnMAML1 is likely to inhibit juxtacrine-mediated, but not paracrine-mediated[4-6] or cell-autonomous, senescence. These data reinforce the immune-modulating function of Notch expression.

We confirmed the recruitment of immune cells into the liver injected with *$NRAS^{G12V}$*; recruitment of CD3+ T-lymphocytes, but not B220+ B-lymphocytes, was significantly accelerated in *$NRAS^{G12V}$*-IRES-*dnMAML1* injected livers compared to *$NRAS^{G12V}$*-IRES-*mVenus* injected animals (Fig. 6c, Supplementary Fig. 6F and G).

Leucocyte recruitment to the liver requires a leucocyte adhesion cascade to sinusoidal endothelial cells, which separate the liver parenchyma from sinusoidal blood flow[34]. To examine the effect of NOTCH1-modulated

secretomes upon lymphocyte recruitment, we performed an in vitro flow adhesion assay[35]: Human sinusoidal endothelial cells (HSECs), derived from explanted livers, were incubated in differentially conditioned media (CM) from IMR90 cells, prior to analysis of the ability of peripheral blood lymphocytes (PBLs) from healthy volunteers to adhere to HSECs under conditions of shear stress, recapitulating the physiological context of liver sinusoids (Supplementary Fig. 7A, B). CM from late phase (d6) of RIS IMR90 cells led to a significant increase in PBL adherence to HSECs and this effect was abrogated by co-expression of N1ICD (Fig. 6e). Similarly, inhibition of the NOTCH-regulated secretome at RIS transition (d3) led to significant increases in PBL adherence to HSEC when compared to $HRAS^{G12V}$-conditioned medium (Fig. 6e). Therefore, RIS-driven secreted factor(s) act upon HSECs to facilitate lymphocyte adhesion, which is negatively regulated by NOTCH through modulation of the SASP.

We next injected *$NRAS^{G12V}$* or *$NRAS^{G12V}$*-IRES-*N1ICD* into mice; surprisingly, the number of NRAS-positive hepatocytes was much lower in the presence of ectopic N1ICD even at d6 (Fig. 7a). To understand potential reasons for this, we stained the livers for cleaved Caspase 3 (CC3), an apoptosis marker, and found hepatocytes expressing *$NRAS^{G12V}$*-IRES-*N1ICD* were often CC3-positive (Fig. 7b, c). Nevertheless, in longer-term cohorts, most *$NRAS^{G12V}$*-IRES-*N1ICD*-, but no *$NRAS^{G12V}$*-,injected mice developed liver tumours (Fig. 7d, e, f). Thus, despite the efficient induction of apoptosis, ectopic $NRAS^{G12V}$ and N1ICD cooperate to drive tumorigenesis. It remains to be elucidated whether this tumour formation is due to escape from senescence arrest

and/or senescence surveillance, but the results underscore the context-dependent interaction between RAS and NOTCH signalling during tumorigenesis.

Our data collectively suggest that, at the endogenous level, Notch signalling modulates SASP composition in senescent hepatocytes, controlling the immune reaction in the liver and thereby negatively regulating the elimination of senescent hepatocytes, at least in part through suppressing T-lymphocyte recruitment to the liver.

NOTCH1 regulates senescence secretome through repression of C/EBPβ

To examine how NOTCH1 controls secretome composition, we measured the impact of N1ICD on two TFs: NFκB and C/EBPβ, previously shown to cooperatively regulate the SASP[6,21,36]. NFκB activation is primarily regulated through nuclear translocation, and consistent with previous studies[20,36], the level of chromatin-bound RELA/p65, the major component of NF B, was increased in RIS cells with its level in whole cell lysates being unchanged (Fig. 8a). In distinction, C/EBPβ was upregulated in both whole cell and chromatin fractions during RIS (Fig. 8a)[6,21,36]. Strikingly, ectopic N1ICD expression diminished levels of C/EBPβ, but not RELA, in both whole and chromatin fractions in RIS cells (Fig. 8a, compare lanes 2 and 4), although ectopic N1ICD appeared to be sufficient to inhibit the basal level of chromatin-bound RELA (Fig. 8a, compare lanes 1 and 3, Supplementary Fig. 8A).

In addition, N1ICD-mediated repression of C/EBPβ was abrogated in the presence of dnMAML1 (Fig. 8b). GSEA revealed enrichment of a C/EBPβ-signature[37] in NIS or N+RIS-downregulated genes, and RIS-upregulated genes (Supplementary Fig. 8B), suggesting that the transcriptional activity of C/EBPβ is broadly diminished in N1ICD-expressing IMR90 cells.

CEBPB translates from different in-frame start sites generating two transcriptional activators, LAP* and LAP (Liver-activating protein), and an N-terminally truncated transcriptional inhibitor, LIP (Liver inhibitory protein)[6]. We introduced full length *CEBPB* cDNA (LAP*, see METHODS) [6], to inducible N1ICD-expressing IMR90 cells. The enforced expression of LAP* in N1ICD-expressing cells fully restored expression of IL-8 (Fig. 8c, compare lanes 2 and 4) and *IL1A* (Fig. 8d), suggesting that repression of pro-inflammatory cytokines by N1ICD is primarily mediated by inhibition of C/EBPβ, although we do not exclude a role for N1ICD in qualitative regulation of the NF B pathway.

The preferential downregulation of C/EBPβ was also observed when IMR90 cells were treated with recombinant TNF-α. Ectopic N1ICD, which inhibited TNF-α-mediated pro-inflammatory cytokine induction, had no effect on the level of TNF-α-activated RELA (Fig. 8e) or other NF B family components (Supplementary Fig. 8C), whereas N1ICD efficiently downregulated C/EBPβ in both basal and TNF-α-treated conditions. Further, ectopic N1ICD-driven downregulation of C/EBPβ was also observed in the HaCaT cells, where

N1ICD failed to induce senescence, suggesting that NOTCH1-mediated C/EBPβ inhibition is not limited to senescence (Supplementary Fig. 8D).

It is well established that IL-1α acutely activates NFκB and C/EBPβ to induce their targets, including *IL1B*, *IL6*, and *IL8*[38]. In the context of senescence, it was shown that IL-1α is an upstream SASP effector, regulating a cytokine network through NFκB and C/EBPβ[21]. Thus, it is possible that N1ICD negatively regulates IL-1α and thereby C/EBPβ. However, overexpression of C/EBPβ was sufficient for inducing *IL1A* even in the presence of ectopic N1ICD (Fig. 8d). In addition, when we treated N1ICD-expressing cells with recombinant IL-1α, we observed only a modest increase of C/EBPβ levels, whereas IL-6 was strongly upregulated to a level higher than control cells (Fig. 8f), suggesting that IL-1α, like IL-1β/6/8, is also downstream of C/EBPβ.

Unlike *IL1B/6/8*, the transcriptional regulation of *IL1A* is unclear. To test whether C/EBPβ directly regulates *IL1A* expression during senescence, we first characterised the basal profile of C/EBPβ binding sites along with key epigenetic marks in IMR90 cells using external datasets[39,40]. We found several C/EBPβ peaks around the *IL1A* locus, including a modest 'proximal' C/EBPβ peak at the transcriptional start site (TSS) and a prominent 'distal' site ~8kb upstream of the TSS (Supplementary Fig. 8E). The proximal and distal sites were enriched for promoter and enhancer markers, respectively (Supplementary Fig. 8E). Interestingly, these two sites were recently identified as a promoter-enhancer pair, forming a looping interaction[41], suggesting that this distal site is an enhancer for *IL1A*. Next, we performed C/EBPβ ChIP-

qPCR, targeting these two regulatory regions of *IL1A*, as well as known C/EBPβ binding sites at the *IL6/8* loci in IMR90 cells expressing N1ICD, $HRAS^{G12V}$, or both. Consistent with previous reports[6], C/EBPβ promoter binding at the *IL6/8* loci was increased in RIS cells (Supplementary Fig. 8F). Similarly, we found that C/EBPβ binding at promoter and, more prominently, enhancer regions of *IL1A* was also increased (Fig. 8g), reinforcing that *IL1A* is a direct C/EBPβ target. In addition, co-expression of N1ICD resulted in reduced enrichment of C/EBPβ at these regulatory regions in the context of $HRAS^{G12V}$ (Fig. 8g). We propose that NOTCH1 inhibits pro-inflammatory cytokines, including IL-1α, primarily through repression of their C/EBPβ-mediated transcription (Fig. 8h).

DISCUSSION

The data that we present here suggests that the SASP is not a singular entity, but a complex evolving entity with tightly regulated composition and spatial activity, dependent upon levels of NOTCH activity. We provide evidence for an additional layer of non-autonomous activity of senescence: 'lateral induction', which was originally described in NOTCH-mediated control of boundary formation during embryonic development[25]. Interestingly, recent studies have identified embryonic senescence as a mechanism for developmental patterning: these senescent cells are accompanied by upregulation of TGF-β signalling and subsequent immune-clearance [42,43].

Another TF involved in embryonic development, GATA4, positively regulates the SASP in part through upregulation of IL-1α[44] and NOTCH signalling

appears to have a negative impact on GATA4 [45]. It would also be interesting to test whether GATA4 plays a role in NOTCH-mediated inhibition of the C/EBPβ-IL1a axis. Additional implications of our data include a possibility that constitutively active NOTCH signalling in tumour cells drive lateral induction of senescence in the stroma. Emerging evidence suggests the important role of bone marrow stroma in survival/maintenance of T-cell ALL, which is associated with activating mutations of NOTCH1[46]. It would be important to test whether NOTCH signalling derived from T-ALL cells can induce NIS-like phenotype in the bone marrow stromal cells, which might have a substantial impact on the T-ALL niche.

Finally, therapeutic elimination of senescent cells has been suggested to provide beneficial effects on tissue homeostasis or tumour suppression[7,8,47,48]. Manipulation of NOTCH may provide a unique therapeutic opportunity for targeting senescent cells through modulation of senescence surveillance.

AUTHOR CONTRIBUTIONS

MH and MN designed the experiments; MH, YI and AJP carried out the in vitro experiments; MPW, NJM and RA performed and analysed the proteomics experiments; MH and TWK performed and analysed the in vivo experiments; DAP and SS performed the HSEC experiments; SM and RS performed bioinformatic analysis; KT provided reagents; WH performed the analysis of immunohistochemistry images. PJL, LZ and MN provided resources; MH and MN wrote the manuscript; all authors reviewed and edited the manuscript.

ACKNOWLEDGEMENTS

We are very grateful to Jesus Gil, Adrian Harris, Daniel Peeper for reagents; Jodi Miller and Leigh-Anne McDuffus for assistance with the immunohistochemistry; Eva Serrao and Kevin Brindle for the murine pancreatic tissue; Guy Slater for analysis of the *IL1A* locus; Matt Clayton for the tail-vein injections; Andrew Young and Masako Narita for technical support. This work was supported by the University of Cambridge, Cancer Research UK and Hutchison Whampoa. Narita laboratory is supported by Cancer Research UK Cambridge Institute Core Grant (C14303/A17197). MH was supported by CRUK Translational Medicine Research Fellowship and CRUK Clinician Scientist Fellowship (C52489/A19924). MPW was supported by a Wellcome Trust Senior Fellowship (108070); SS was funded by a Wellcome Trust Intermediate Fellowship (097162/Z/11/Z). PL was funded by the Wellcome Trust. LZ was funded by the German Research Foundation (DFG; grants FOR2314 and SFB685), the Gottfried Wilhelm Leibniz Program, the European Research Council (projects 'CholangioConcept'), the German Ministry for Education and Research (BMBF) (eMed-Multiscale HCC), the German Universities Excellence Initiative (third funding line: 'future concept'), the German Center for Translational Cancer Research (DKTK) and the German–Israeli Cooperation in Cancer Research (DKFZ–MOST).

REFERENCES

1. Campisi, J. Aging, cellular senescence, and cancer. *Annu. Rev. Physiol.* **75,** 685–705 (2013).
2. Kuilman, T. & Peeper, D. S. Senescence-messaging secretome: SMS-ing cellular stress. *Nat. Rev. Cancer* **9,** 81–94 (2009).

3. Childs, B. G., Durik, M., Baker, D. J. & van Deursen, J. M. Cellular senescence in aging and age-related disease: from mechanisms to therapy. *Nat. Medicine* **21,** 1424–1435 (2015).
4. Acosta, J. C. *et al.* A complex secretory program orchestrated by the inflammasome controls paracrine senescence. *Nat. Cell Biol.* **15,** 978–990 (2013).
5. Hubackova, S., Krejcikova, K., Bartek, J. & Hodny, Z. IL1- and TGFβ-Nox4 signaling, oxidative stress and DNA damage response are shared features of replicative, oncogene-induced, and drug-induced paracrine 'Bystander senescence'. *Aging (Albany NY)* **4,** 932–951 (2012).
6. Kuilman, T. *et al.* Oncogene-induced senescence relayed by an interleukin-dependent inflammatory network. *Cell* **133,** 1019–1031 (2008).
7. Krizhanovsky, V. *et al.* Senescence of activated stellate cells limits liver fibrosis. *Cell* **134,** 657–667 (2008).
8. Kang, T.-W. *et al.* Senescence surveillance of pre-malignant hepatocytes limits liver cancer development. *Nature* **479,** 547–551 (2011).
9. Xue, W. *et al.* Senescence and tumour clearance is triggered by p53 restoration in murine liver carcinomas. *Nature* **445,** 656–660 (2007).
10. Krtolica, A., Parrinello, S., Lockett, S., Desprez, P. Y. & Campisi, J. Senescent fibroblasts promote epithelial cell growth and tumorigenesis: a link between cancer and aging. *Proc. Natl Acad. Sci. USA* **98,** 12072–12077 (2001).
11. Coppé, J.-P. *et al.* Senescence-associated secretory phenotypes reveal cell-nonautonomous functions of oncogenic RAS and the p53 tumor suppressor. *Plos Biol.* **6,** 2853–2868 (2008).
12. Kopan, R. & Ilagan, M. X. G. The canonical Notch signaling pathway: unfolding the activation mechanism. *Cell* **137,** 216–233 (2009).
13. Ntziachristos, P., Lim, J. S., Sage, J. & Aifantis, I. From Fly Wings to Targeted Cancer Therapies: A Centennial for Notch Signaling. *Cancer Cell* **25,** 318–334 (2014).
14. Weekes, M. P. *et al.* Latency-associated degradation of the MRP1 drug transporter during latent human cytomegalovirus infection. *Science* **340,** 199–202 (2013).
15. Young, A. R. J. *et al.* Autophagy mediates the mitotic senescence transition. *Genes Dev.* **23,** 798–803 (2009).
16. Cui, H., Kong, Y., Xu, M. & Zhang, H. Notch3 functions as a tumor suppressor by controlling cellular senescence. *Cancer Res.* **73,** 3451–3459 (2013).
17. Kagawa, S. *et al.* Cellular senescence checkpoint function determines differential Notch1-dependent oncogenic and tumor-suppressor activities. *Oncogene* **34,** 2347–2359 (2015).
18. Procopio, M.-G. *et al.* Combined CSL and p53 downregulation promotes cancer-associated fibroblast activation. *Nat. Cell Biol.* **17,** 1193–1204 (2015).
19. Kirschner, K. *et al.* Phenotype Specific Analyses Reveal Distinct Regulatory Mechanism for Chronically Activated p53. *PLoS Genet.* **11,** e1005053 (2015).
20. Acosta, J. C. *et al.* Chemokine signaling via the CXCR2 receptor

reinforces senescence. *Cell* **133,** 1006–1018 (2008).
21. Orjalo, A. V., Bhaumik, D., Gengler, B. K., Scott, G. K. & Campisi, J. Cell surface-bound IL-1alpha is an upstream regulator of the senescence-associated IL-6/IL-8 cytokine network. *Proc. Natl Acad. Sci. USA* **106,** 17031–17036 (2009).
22. Fryer, C. J., Lamar, E., Turbachova, I., Kintner, C. & Jones, K. A. Mastermind mediates chromatin-specific transcription and turnover of the Notch enhancer complex. *Genes Dev.* **16,** 1397–1411 (2002).
23. Lee, B. Y. *et al.* Senescence-associated beta-galactosidase is lysosomal beta-galactosidase. *Aging Cell* **5,** 187–195 (2006).
24. Hata, A., Lo, R. S., Wotton, D., Lagna, G. & Massague, J. Mutations increasing autoinhibition inactivate tumour suppressors Smad2 and Smad4. *Nature* **388,** 82–87 (1997).
25. Lewis, J. Notch signalling and the control of cell fate choices in vertebrates. *Semin. Cell Dev. Biol.* **9,** 583–589 (1998).
26. Hartman, B. H., Reh, T. A. & Bermingham-McDonogh, O. Notch signaling specifies prosensory domains via lateral induction in the developing mammalian inner ear. *Proc. Natl Acad. Sci. USA* **107,** 15792–15797 (2010).
27. D'Souza, B., Miyamoto, A. & Weinmaster, G. The many facets of Notch ligands. *Oncogene* **27,** 5148–5167 (2008).
28. Kurpinski, K. *et al.* Transforming growth factor-beta and notch signaling mediate stem cell differentiation into smooth muscle cells. *Stem Cells* **28,** 734–742 (2010).
29. Collado, M. *et al.* Tumour biology: senescence in premalignant tumours. *Nature* **436,** 642 (2005).
30. Hingorani, S. R. *et al.* Preinvasive and invasive ductal pancreatic cancer and its early detection in the mouse. *Cancer Cell* **4,** 437–450 (2003).
31. Miyamoto, Y. *et al.* Notch mediates TGF alpha-induced changes in epithelial differentiation during pancreatic tumorigenesis. *Cancer Cell* **3,** 565–576 (2003).
32. Avila, J. L. & Kissil, J. L. Notch signaling in pancreatic cancer: oncogene or tumor suppressor? *Trends Mol. Med.* **19,** 320–327 (2013).
33. Caldwell, M. E. *et al.* Cellular features of senescence during the evolution of human and murine ductal pancreatic cancer. *Oncogene* **31,** 1599–1608 (2011).
34. Lee, W.-Y. & Kubes, P. Leukocyte adhesion in the liver: distinct adhesion paradigm from other organs. *J. Hepatol.* **48,** 504–512 (2008).
35. Shetty, S., Weston, C. J., Adams, D. H. & Lalor, P. F. A flow adhesion assay to study leucocyte recruitment to human hepatic sinusoidal endothelium under conditions of shear stress. *J. Vis. Exp.* (2014). doi:10.3791/51330
36. Chien, Y. *et al.* Control of the senescence-associated secretory phenotype by NF-κB promotes senescence and enhances chemosensitivity. *Genes Dev.* **25,** 2125–2136 (2011).
37. Huggins, C. J. *et al.* C/EBPγ suppresses senescence and inflammatory gene expression by heterodimerizing with C/EBPβ. *Mol. Cell. Biol.* **33,** 3242–3258 (2013).
38. Nakazato, Y. *et al.* Interleukin (IL)-1 and IL-4 synergistically stimulate NF-IL6 activity and IL-6 production in human mesangial cells. *Kidney*

Int. **54,** 71–79 (1998).
39. ENCODE Project Consortium. An integrated encyclopedia of DNA elements in the human genome. *Nature* **489,** 57–74 (2012).
40. Roadmap Epigenomics Consortium *et al.* Integrative analysis of 111 reference human epigenomes. *Nature* **518,** 317–330 (2015).
41. Jin, F. *et al.* A high-resolution map of the three-dimensional chromatin interactome in human cells. *Nature* **503,** 290–294 (2013).
42. Storer, M. *et al.* Senescence Is a Developmental Mechanism that Contributes to Embryonic Growth and Patterning. *Cell* (2013). doi:10.1016/j.cell.2013.10.041
43. Muñoz-Espín, D. *et al.* Programmed Cell Senescence during Mammalian Embryonic Development. *Cell* (2013). doi:10.1016/j.cell.2013.10.019
44. Kang, C. *et al.* The DNA damage response induces inflammation and senescence by inhibiting autophagy of GATA4. *Science* **349,** aaa5612 (2015).
45. Boni, A. *et al.* Notch1 regulates the fate of cardiac progenitor cells. *Proc. Natl Acad. Sci. USA* **105,** 15529–15534 (2008).
46. Pitt, L. A. *et al.* CXCL12-Producing Vascular Endothelial Niches Control Acute T Cell Leukemia Maintenance. *Cancer Cell* **27,** 755–768 (2015).
47. Baker, D. J. *et al.* Clearance of p16Ink4a-positive senescent cells delays ageing-associated disorders. *Nature* **479,** 232–236 (2011).
48. Dörr, J. R. *et al.* Synthetic lethal metabolic targeting of cellular senescence in cancer therapy. *Nature* **501,** 421–425 (2013).

FIGURE LEGENDS

Figure 1. Plasma membrane proteomics (PMP) defines NOTCH1 as upregulated in OIS. (a) The workflow for quantitative PMP using differential SILAC labelling of growing and $HRAS^{G12V}$-induced senescent (RIS) IMR90 cells. (b) GO cellular compartment term enrichment for all 1502 identified proteins in both conditions. (c) Volcano plot of 521 high-confidence protein identifications from PMP demonstrating $\log_2$ fold change (RIS(d6) / Growing) against negative $\log_{10}$ p value (n = 4 independent experiments). Among 167 proteins differentially expressed during RIS ($p<0.05$), red dots indicate 94 proteins with more than two fold change. (d) Cell surface NOTCH1 expression by flow-cytometry in indicated IMR90 cells: left, ER:$HRAS^{G12V}$ cells with (d6) or without (Growing) 4OHT, iso-IgG, isotype control IgG; centre, cells with constitutive overexpression of either $HRAS^{G12V}$, E1A, or both; right, DNA damage-induced senescence (DDIS). To establish DDIS, cells were treated with 100μM Etoposide for 2 days, followed by 5-days incubation in drug-free medium.

Figure 2. Dynamic canonical NOTCH1 signalling is responsible for reciprocal regulation of TGF-β ligands and pro-inflammatory cytokines during senescence. (a) Time series analysis of cell surface NOTCH1 expression during RIS in IMR90 cells by flow cytometry. Values are means relative to d0 ± SEM; n = 3. (b and c) Time course of protein expression by immunoblotting during RIS (b) or DDIS (c). (d) ER:$HRAS^{G12V}$ IMR90 cells, expressing dnMAML1-mVenus or matched control, were incubated with or without 4OHT for 3 days and analysed for expression of indicated mRNA and

proteins by qRT-PCR and immunoblotting respectively; n ≥ 4; unpaired T-test. (e) ER:HRAS^{G12V} IMR90 cells, expressing a doxycycline-inducible N1ICD-FLAG construct (TRE-N1ICD) were analysed after 6 days treatment with 4OHT with or without doxycycline at indicated concentrations from d3 by qRT-PCR and immunoblotting; n = 5; unpaired T-test. Values are mean ± SEM; *P ≤ 0.05, **P ≤ 0.01, ***P ≤ 0.001. Statistics source data for a, d & e are provided in Supplementary Table 2.

Figure 3. NOTCH1 drives a cell-autonomous senescence with a distinct secretory profile. (a and b) ER:HRAS^{G12V} IMR90 cells, stably expressing N1ICD-FLAG or control vector (V), were incubated with or without 4OHT for 6 days and analysed for expression of indicated proteins by immunoblotting (a), SA-β-gal and BrdU incorporation (b). One way ANOVA with Dunnett's multiple comparison test; bars are means of ≥200 cells, n = 4. ***P ≤ 0.001 versus control cells. Scale bar 100μm. (c) Time series analysis of indicated transcripts after doxycycline (Doxy) induction in TRE-N1ICD-FLAG IMR90 cells by qRT-PCR. Values are mean ± SEM, n = 3. Inset, immunoblotting of fractionated chromatin in IMR90 cells expressing HRAS^{G12V} (d6) or TRE-N1ICD-FLAG (d3) for downstream TGF-β phosphorylation-target SMAD3 (phos-SMAD3). (d) TRE-N1ICD-mVenus IMR90 cells with or without 3 days of doxycycline were analysed for cell surface expression of the TGFB1 gene product latency-associated peptide by flow cytometry. (e) Differentially expressed transcripts in N1ICD-, HRAS^{G12V}- or Etoposide-induced senescent IMR90 cells (NIS, RIS, or DDIS, respectively), compared to normal control cells. Heat map shows z-score normalised fold changes of 1150 secretome

genes differentially expressed in at least in one comparison. Representative KEGG pathways enriched in four clusters (False discovery rate (FDR) < 0.01) are shown. (f) TRE-N1ICD-FLAG IMR90 cells treated with or without doxycycline for 3 days with or without TGF-β receptor antagonists (#1, SB431542; #2, A83-01) were analysed by qRT-PCR and immunoblotting for the indicated mRNA and proteins in addition to proliferation and cell cycle analyses. Values are mean ± SEM, n ≥ 3. Statistics source data for b, c & f are provided in Supplementary Table 2.

Figure 4. NOTCH1 drives non-cell-autonomous senescence partly dependent upon TGF-β. (a) The proliferative ability of mRFP cells was analysed during co-culture with unlabelled senescent cells by proliferation analysis; representative images demonstrating co-cultured cells. Scale bar 150 μm. NIS, doxycycline was added at d0 to induce N1ICD; RIS, ER:HRAS^{G12V} was pre-induced for 4 days before co-culture; DDIS, senescence was induced by etoposide as in Figure 2C for 4 days before co-culture. (b) mRFP cells were co-cultured with doxycycline-inducible TRE-N1ICD cells treated with or without doxycycline for 3 days prior to flow sorting and expression analysis of the 2 cell populations for the indicated transcripts by qRT-PCR; unpaired T-test; bars are means, n = 3. (c) The proliferative ability of mRFP IMR90 cells was analysed during co-culture with TRE-N1ICD IMR90 cells treated with or without doxycycline and TGF-β receptor antagonists; representative result from n = 5. (d and e) mRFP (puromycin-resistant) cells were co-cultured with cells stably expressing N1ICD-FLAG (hygromycin-resistant) for 7 days prior to puromycin selection to selectively

remove N1ICD-expressing cells, yielding populations that were ~99% mRFP-positive by flow cytometry. mRFP cells were then analysed for expression of indicated proteins by immunoblotting (d), SA-β-gal and DNA synthesis by BrdU incorporation (e); unpaired T-test; values are mean ± SEM of ≥200 cells from 8 high power fields, n = 7. *$P \leq 0.05$, **$P \leq 0.01$, ***$P \leq 0.001$. Scale bar 200 μm. Statistics source data for b & e are provided in Supplementary Table 2.

Figure 5. NOTCH1 drives juxtacrine senescence through JAG1-mediated lateral induction in IMR90 cells. (a) Time series analysis of JAG1 expression by immunoblotting (upper) and at the cell surface by flow cytometry (lower) after doxycycline induction in TRE-N1ICD cells. (b) The proliferative ability of mRFP cells was analysed during co-culture with TRE-N1ICD cells treated with or without doxycycline and the gamma secretase inhibitor DAPT at indicated concentrations; representative result from n = 4. (c) The proliferative ability of TRE-N1ICD cells was analysed with or without doxycycline and DAPT at indicated concentrations; representative result from n = 4. (d) The proliferative ability of mRFP cells with stable expression of dnMAML1-mVenus or mVenus alone was analysed during co-culture with TRE-N1ICD cells treated with or without doxycycline; representative result from n = 4. (e and f) Expression of JAG1 and proliferation of TRE-N1ICD cells stably expressing vector or indicated shRNAs targeting JAG1, demonstrated by immunoblot (e) and proliferation analysis with or without doxycycline (f); representative result from n = 4. (g) The proliferative ability of mRFP cells was analysed during co-culture with TRE-N1ICD cells with or without sh-JAG1 and

with or without doxycycline. (h) mRFP cells were analysed for BrdU incorporation, when physically separated from TRE-N1ICD cells treated with or without doxycycline in a transwell chamber; unpaired T-test; ≥200 cells from 8 high power fields; n = 5. (i) TRE-N1ICD cells treated with or without doxycycline and TGF-β receptor antagonists (left) or co-transfected with vector or dnSMAD4 (right) were analysed for *JAG1* expression by qRT-PCR; n = 3; 1, SB431542; 2, A83-01. One way ANOVA with Dunnett's multiple comparison test (left) or unpaired t-test (right); bars are means (h and i) ± SEM (h). Statistics source data for h & i are provided in Supplementary Table 2.

Figure 6. NOTCH1 is dynamically upregulated within NRAS-senescent hepatocytes and inhibits senescence surveillance. (a) Livers were harvested from mice 12 days after hydrodynamic tail vein injection of $NRAS^{G12V}$ or inactive $NRAS^{G12V/D38A}$-bearing transposons and analysed by immunohistochemistry for NRAS and Notch1 expression in serial sections; Quantification of NRAS+ hepatocytes expressing NOTCH1; values are mean ± SEM from manual counting of ≥200 cells; n = 3 mice per condition. Insets, magnified pictures of dotted rectangular areas. Scale bar 200 μm. (b) Time series analysis of hepatic NRAS-expression by immunohistochemistry after injection of $NRAS^{G12V}$(-IRES-mVenus) or $NRAS^{G12V}$-IRES-dnMAML1(-mVenus). Scale bar 200 μm. (c) Quantification of NRAS, p21, or CD3 (T-lymphocyte marker) positive cells within livers of mice treated as in (b); unpaired T-test; values are mean ± SEM from manual counting (NRAS) or automated image analysis of ≥10^5 cells (p21 / CD3) from liver sections (see

METHODS); n ≥ 3 mice per condition; *P ≤ 0.05, **P ≤ 0.01. (d) Lateral induction of Notch signalling in mouse livers treated as in (b). Representative immunohistochemistry of NRAS and Hes1 at d9 in serial sections. Insets, magnified pictures of dotted rectangle areas. Asterisk demonstrates Hes1-expressing, NRAS-negative cells adjacent to NRAS-expressing hepatocytes. Arrowheads demonstrate positive internal control staining of Hes1 within cholangiocytes. The percentage of NRAS-positive cells with adjacent Hes1-positive (but not NRAS) were manually counted; n = 3 mice per condition; bars are means; unpaired T-test. Similar results were also obtained using dual staining in the same section (Supplemental Fig. 6C). Scale bar 200 μm. (e) Flow-based assay of peripheral blood lymphocyte (PBL) adherence (cells/mm^2/10^6) to human liver sinusoidal endothelial cells (HSEC) from 3 separate individuals pre-incubated with conditioned media (CM) from IMR90 cells expressing ER:HRASG12V and TRE-N1ICD with or without 4OHT (d6) and/or doxycycline (d3) (left; n = 3); or CM from ER:HRASG12V IMR90 cells, expressing dnMAML1-mVenus or matched control and incubated with or without 4OHT for 3 days (right; n = 3) (see Supplementary Fig. 7A, B). Representative images (bottom) demonstrating adherent PBLs (arrows) to HSEC after pre-incubation with indicated CM. One way ANOVA with Dunnett's multiple comparison test; bars are mean; *P ≤ 0.05, **P ≤ 0.01. Scale bar 50μm. Statistics source data for a, c, d & e are provided in Supplementary Table 2.

Figure 7. Co-expression of $NRAS^{G12V}$ and N1ICD drives short-term apoptosis and long-term tumourigenesis in the liver. (a-c) Livers from

mice injected with either $NRAS^{G12V}$ (n = 10) or $NRAS^{G12V}$-IRES-N1ICD (n = 11) were subjected to IHC for NRAS and cleaved caspase 3 staining at the indicated time points in serial sections. Relatively fewer NRAS-positive hepatocytes were detected in the $NRAS^{G12V}$-IRES-N1ICD cohort (d6 (n = 4) and d12 (n = 7)) (a), and these NRAS-positive cells were mostly positive for cleaved caspase 3 (d6) (b, c). Insets are magnified pictures of dotted rectangular areas (b). Bars are means from automated image analysis of $\geq 10^5$ cells from each liver section; n ≥ 4 mice per condition; unpaired t-test. Scale bar 200 μm. (d) Mice injected with $NRAS^{G12V}$ (n = 7) or $NRAS^{G12V}$-IRES-N1ICD (n = 9) underwent long-term follow-up; necropsy was performed in all to confirm the presence of liver tumours. Kaplan-Meier plots of cancer-free survival from the 2 cohorts; survival analysis by Log-rank test. (e) Example images of gross liver pathology at 2 months post-HDTV injection of one mouse from each cohort revealing a large tumour (long black arrow) and multiple small cystic lesions in the liver injected with $NRAS^{G12V}$-IRES-N1ICD. (f - g) Immunohistochemical and H&E staining of serial liver sections from each cohort for the indicated proteins. H&E staining demonstrating tumour (T) infiltrating the surrounding normal parenchyma (N) and strong tumoural immunohistochemical staining for the proliferative marker ki67 in serial sections (g). Images in (g) are magnified views of dotted rectangular areas in (f). *P ≤ 0.05, **P ≤ 0.01. Scale bar upper panels 5mm, lower panels 200 μm. Statistics source data for a & c are provided in Supplementary Table 2.

Figure 8. NOTCH1 controls the pro-inflammatory SASP through repression of C/EBPβ. (a) ER:$HRAS^{G12V}$/TRE-N1ICD-FLAG IMR90 cells

877 treated with or without 6 days of 4OHT and 3 days of doxycycline were
878 analysed for expression of RELA and C/EBPβ in whole cell lysate and
879 fractionated chromatin by immunoblotting. (b) Time series analysis of
880 chromatin-bound N1ICD-FLAG and C/EBPβ after doxycycline treatment of
881 TRE-N1ICD IMR90 cells with or without dnMAML1. (c and d) TRE-N1ICD
882 IMR90 cells with or without ectopic C/EBPβ-LAP* and 3 days of doxycycline
883 treatment were analysed for C/EBPβ, IL-8 (c) and *IL1A* (d) expression by
884 immunoblot and qRT-PCR; n = 3. (e) TRE-N1ICD IMR90 cells treated with or
885 without doxycycline for 3 days, then with or without 100ng/ml TNF-α for 1 hour
886 were analysed for expression and chromatin binding of indicated mRNA and
887 proteins by qRT-PCR and immunoblot respectively; unpaired T-test; n = 3;
888 bars are means. (f) TRE-N1ICD IMR90 cells treated with or without
889 doxycycline for 3 days, and 10ng/ml IL-1α for the final 24 hours were
890 analysed by immunoblotting. (g) ER:HRAS^{G12V}- and TRE-N1ICD-FLAG-
891 expressing IMR90 cells treated with or without 6 days of 4OHT and 3 days of
892 doxycycline were subjected to chromatin immunoprecipitation of endogenous
893 C/EBPβ and subsequent qPCR for proximal and distal sites at the *IL1A* locus
894 (Supplemental Figure 8E and METHODS); n = 3; One way ANOVA with
895 Dunnett's multiple comparison test; values are mean ± SEM. (h) Model for
896 NOTCH-mediated SASP switch during senescence. *$P \leq 0.05$, **$P \leq 0.01$,
897 ***$P \leq 0.001$. Statistics source data for d, e & g are provided in
898 Supplementary Table 2.
899
900

METHODS

Cell culture

IMR90 (ATCC), WI38 (ATCC) and ESFs (embryonic skin fibroblasts)[49] (a kind gift from Dr. Jesus Gil, Imperial College, London) human diploid fibroblasts were cultured as previously described in DMEM /10% fetal calf serum (FCS) in a 5% O_2 / 5% CO_2 atmosphere. hTERT-RPE1 cells (a telomerase-immortalised human retinal pigment epithelial cell line) (ATCC) were grown in DMEM/F12 / 10% FCS in a 5% O_2 / 5% CO_2 atmosphere. HACAT, cells (ATCC) were cultured in DMEM / 10% FCS in a 21% O_2 / 5% CO_2 atmosphere. No cell lines used in this study were found in the database of commonly misidentified cell lines that is maintained by ICLAC and NCBI Biosample. Cell identity was confirmed through STR genotyping. Regular testing was always negative for mycoplasma contamination.

The following drugs and inhibitors were used: 4-hydroxytamoxifen (4OHT) (Sigma); N-[(3,5-Difluorophenyl)acetyl]-L-alanyl-2-phenyl]glycine-1,1-dimethylethyl ester (DAPT) (Sigma); SB431542 (Tocris); A 83-01 (Tocris); GW788388 (Tocris); Etoposide (Sigma); recombinant human TGF-β1 (Cell Signaling); recombinant human TGF-β2 (Peprotech); recombinant human TGF-β3 (Peprotech); Tumor necrosis factor alpha (TNF-α); recombinant IL-1α (both R&D systems).

Vectors

The following retroviral vectors were used in this study: pBabe-puro for $HRAS^{G12V50}$, C/EBPβ-LAP* (alternative start codons were replaced with TTG;

a kind gift from Dr. Daniel Peeper, NKI, Amsterdam)[6]; pLNCX2 (Clontech) for ER:HRAS^{G12V15}; pLNCX (Clontech) for ΔMEK1:ER (ΔN3, S218E, S222D)[51]; pWZL-hygro for N1ICD-FLAG (residues 1758 – 2556 of human NOTCH1, as described[52]), mRFP1; pLPC-puro for dnMAML1-mVenus (residues 12 – 74 of human MAML1), N1ICD-FLAG, mRFP1; pQCXIH-i N1ICD-FLAG, N1ICD-FLAG-mVenus, C/EBPβ-LAP*, dnSMAD4-mVenus (residues 1 - 514 of human SMAD4, as described [24]); pQCXIN-i for N1ICD-FLAG; pMSCV-miR30-puro for shJAG1 (target sequences: #1, 5'-GCGTGACCTGTGATGACTACT-3'; and #4, 5'-GGTCTTTGAGCTCCCACTTCT-3').

The tetracycline-inducible retroviral vectors (pQCXIH-i and pQCXIN-i) were cloned using the following strategies. A third generation tet-responsible element (TRE3G) and a constitutively expressed rtTA3 tet-transactivator cassette were PCR-amplified from pCLIIP-i[19]. These two fragments were assembled by overlap-extension PCR and the product was cloned into pQCXIH or pQCXIN (Clontech).

Plasmids for Hydrodynamic tail-vein injection: pPGK-SB13, pT/CAGGS for NRAS^{G12V}, NRAS$^{G12V/D38A8}$, NRAS^{G12V}-IRES-mVenus, NRAS^{G12V}-IRES-dnMAML1-mVenus, NRAS^{G12V}-IRES-N1ICD-FLAG).

SILAC labelling

Cells were cultured in SILAC DMEM (Thermo) supplemented with 10% dialysed FCS (Life Technologies), L-proline (280mg/l, Sigma), L-glutamine (Life technologies) and either light (Arg 0, Lys 0) (Sigma), medium (Arg 6, Lys

4) or heavy (Arg 10 Lys 8) amino acids (CKGas) at 150mg/l and 85mg/l for lysine and arginine respectively. Cells were cultured for 9 days to allow complete labelling of the proteome with the appropriate amino acids before induction of senescence.

Plasma membrane proteomics

PMP was performed as described previously[14]. Briefly, surface sialic acid residues were oxidised, biotinylated with aminooxy-biotin (Biotium), and biotinylated cells incubated in a 1% Triton X-100 lysis buffer. Biotinylated glycoproteins were enriched with high affinity streptavidin agarose beads (Pierce) and washed extensively. Captured protein was reduced and alkylated then digested with trypsin on-bead overnight. Tryptic peptides were collected and fractionated. Glycopeptides were eluted using PNGase (New England Biolabs).

High pH reverse-phase high pressure liquid chromatography (HpRP-HPLC) was performed on tryptic peptides as described previously[14]. LC-MSMS was performed using a NanoAcquity uPLC (Waters, MA, USA) coupled to an LTQ-OrbiTrap XL (Thermo, FL, UA). Raw MS files were processed using MaxQuant version 1.3.0.5[53]. Reversed decoy databases were used and the false discovery rate for both peptides and proteins were set at 0.01. Protein quantitation utilised razor and unique peptides and required a minimum of 2 ratio counts, with normalised protein ratios reported. Significance B values were calculated. We assessed the number of PM proteins identified as described previously[14].

Proteomic Analysis

Proteins were selected for differential expression analysis such that they had been quantified in at least two replicates, and that at least one of these quantifications was based on more than one peptide. A single sample t-test was then applied to the mean $\log_2$ fold change values to assess whether these were significantly different to zero. Proteins were selected as significantly differentially expressed if p value <0.05. All detected proteins were used for enrichment testing of GO localisation (Cellular Component) terms using Metacore (Thomson Reuters). 'High confidence' was defined as follows: peptides identified in at least 2 independent replicates with at least 1 replicate having 2 or more peptides.

Expression profiling by mRNA sequencing

RNA was extracted using the Qiagen RNeasy plus kit according to manufacturer's instructions and RNA quality checked using a Bioanalyser Eukaryote Total RNA Nano Series II chip (Agilent). mRNASeq libraries were prepared from at least 6 biological replicates of each condition using the TruSeq Stranded mRNA Library Prep Kit (Illumina) according to the manufacturers instructions. Single-end 40bp reads generated on the Illumina HiSeq were aligned to the human genome version GRCh37.64 using TopHat v2.0.4[54]. Read counts were then obtained using HTSeq-count v0.5.3p9 (http://www-huber.embl.de/users/anders/HTSeq/doc/overview.html), normalised and tested for differential gene expression using the Bioconductor package DESeq v1.10.1[55]. Multiple testing correction was applied using the

Benjamini-Hochberg method. Genes were selected as differentially expressed with a false discovery rate (FDR) of <0.01. Secretome genes were defined as previously described[56].

Network analysis of proteomic and transcriptomic data

RIS-associated PMP data complemented by mRNA-Seq expression data were used to identify key senescence-associated membrane protein network hubs. Proteins detected through PMP were merged with genes, but genes annotated in the cellular membrane compartment were excluded. Log_2 fold ratios were used for both proteomics and transcriptomic data. Data were analysed using Ingenuity Pathway Analysis (IPA) (QIAGEN); the possible interaction networks were generated using Ingenuity knowledge base and included only direct relationships. Default settings were used, apart from restricting the networks to experimentally observed interactions in human data. The highest scoring network as assigned by IPA, presented here, highlighted the importance of NOTCH1 as a key hub in the PMP data. For graph readability we removed interactions from non-hub genes.

Chromatin isolation

Chromatin isolation was performed as described previously[50].

BrdU incorporation, colony formation and SA-β-gal assays

Cellular proliferation by BrdU incorporation, colony formation and SA-β-gal analysis have been described previously[50].

Cellular proliferation by Incucyte

Analysis of short-term cellular proliferation was performed in either an Incucyte-HD or Incucyte-Zoom device (Essen Bioscience) in a 21% O_2 atmosphere. Cells were plated, at 4 x 10^5 cells for monoculture or at 3.5 x 10^5 signal-sending cells with 1.5 x 10^5 target cells, in a 12-well plate in 1ml cell culture media. Cell proliferation was determined through repeated measures of confluency on phase or epifluorescent imaging.

Gene set enrichment analyses (GSEA)

GSEA were performed as described[57]. P-values derived from DESeq analyses of the RNA-Seq data were –log10 transformed and then signed according to whether any particular genes was up(+)- or down(-)-regulated compared to control samples. These values were then used for ranking and weighting of genes in subsequent GSEA analyses[58]. Cell-cycle related genesets were obtained from the Molecular Signatures Database (http://software.broadinstitute.org/gsea/msigdb). Other gene signatures used were obtained from datasets in the Gene Expression Omnibus (GEO).

Flow cytometry

Cells were washed once with cold PBS, prior to dissociation with Versene (Life Technologies), washed twice more in PBS / 0.1% Fetal calf serum, blocked in 1% mouse or rabbit serum before incubation with combinations of the following fluorochrome-conjugated antibodies: anti-NOTCH1 (Ebioscience, 17-9889, 1:50); anti-JAGGED1 (R&D systems, FAB1726A, 1:8); anti-latency associated peptide (Ebioscience, 17-9829, 1:20). Cells were then

washed twice more, before fixation with 4% PFA and analysis on a FACSCalibur (Becton Dickenson). Flow-based cell sorting was conducted on a FACSAria II cytometer (Becton Dickenson). Flow data was analysed with FlowJo v10.

Laser Scanning Cytometry

Cell cycle profile analysis was performed using Laser Scanning Cytometry on an iCys Research Imaging Cytometer (CompuCyte, Cambridge, MA) using anti-BrdU (BD, 555627, 1:500) and counter-staining with DAPI.

mRNA expression by quantitative RT-PCR

RNA was extracted using the Qiagen RNeasy plus kit as above and reverse transcribed to cDNA using the high capacity reverse transcription kit (Applied Biosystems). qRT-PCR was performed as described before[50] with relative expression determined by the $2^{-\Delta\Delta Ct}$ method[59] using β-Actin (ACTB) as an internal control. Primer sequences are as follows:

ACTB forward primer GGACTTCGAGCAAGAGATGG

ACTB reverse primer AGGAAGGAAGGCTGGAAGAG

CCNA2 forward primer GCGTTCACCATTCATGTGGA

CCNA2 reverse primer CAGGGCATCTTCACGCTCTATT

CDKN2B forward primer GCGTTCACTCCAATGTCTGCTG

CDKN2B reverse primer TCCACTTTGTCCTCAGTCTTCAGG

CEBPB forward primer CTTCAGCCCGTACCTGGAG

CEBPB reverse primer GGAGAGGAAGTCGTGGTGC

JAG1 forward primer TGGTCAACGGCGAGTCCTTTAC

JAG1 reverse primer GCAGTCATTGGTATTCTGAGCACAG

TGFBI forward primer CCACCATCACCAACAACATCCAG

TGFBI reverse primer GCCGTTACCTTCAAGCATCGTG

IL1A forward primer AACCAGTGCTGCTGAAGGA

IL1A reverse primer TTCTTAGTGCCGTGAGTTTCC

IL1B forward primer CTGTCCTGCGTGTTGAAAGA

IL1B reverse primer TTGGGTAATTTTTGGGATCTACA

IL6 forward primer TGAAAGCAGCAAAGAGGCACTG

IL6 reverse primer TGAATCCAGATTGGAAGCATCC

IL8 forward primer AAGGAAAACTGGGTGCAGAG

IL8 reverse primer: ATTGCATCTGGCAACCCTAC

TGFB1 forward primer CAGAAATACAGCAACAATTCC

TGFB1 reverse primer CTGAAGCAATAGTTGGTGTC

TGFB3 forward primer TGCGTGAGTGGCTGTTGAGAAG

TGFB3 reverse primer CCATTGGGCTGAAAGGTGTGAC

HES1 forward primer ACGTGCGAGGGCGTTAATAC

HES1 reverse primer ATTGATCTGGGTCATGCAGTTG

HEY1 forward primer CCGCTGATAGGTTAGGTCTCATTTG

HEY1 reverse primer TCTTTGTGTTGCTGGGGCTG

Protein expression by immunoblotting and Immunofluorescence

Immunofluorescence and immunoblotting, on SDS-PAGE on gels of various concentrations, were performed as described previously[50]. The following antibodies were used in this study: anti-HRAS (Calbiochem, OP-23, 1:500); Anti-Cyclin A2 (Sigma, C4710, 1:500); anti-NOTCH1 (Cell signaling, 4380,

1:1000); anti-N1ICD (Cell signaling, 4147, 1:500); anti-HES1 (Cell signaling, 11988, 1:1000); anti-TGF-β1 (Cell signaling, 3709, 1:500); anti-IL-6 (R&D systems, MAB2061, 1:250); anti-IL-8 (R&D systems, MAB208, 1:500); anti-β-Actin (Sigma, A5441, 1:5000); anti-GFP (Clontech, 632377, 1:1000); anti-Rb (Cell signaling, 9309, 1:1000); anti-JAGGED1 (Cell signaling, 2155, 1:1000); anti-FLAG (Cell signaling, 2368, 1:1000); anti-C/EBPβ-LAP (Cell signaling, 3087, 1:1000); anti-C/EBPβ (Santa-Cruz, sc-150, 1:500); anti-Histone H3 (Abcam, Ab-1791, 1:10,000); anti-RelA (Cell signaling, 3034, 1:1000); anti-RelB (Cell signaling, 4922, 1:1000); anti-c-Rel (Cell signaling, 4727, 1:1000); anti-NF-kB1 (Cell signaling, 3035, 1:1000); anti-NF-kB2 (Cell signaling, 4882, 1:1000); anti-IkBα (Cell signaling, 4814, 1:1000); anti-phospho-IkBα (Cell signaling, 9246, 1:1000); anti-p16 (Santa-Cruz, sc-759, 1:500); anti-p21 (Santa-Cruz, sc-397, 1:1000); anti-SMAD2/3 (Cell signaling, 8685, 1:1000); anti-phospho-SMAD3 (Abcam, ab52903, 1:1000); anti-TGFB-induced (Cell signalling, 5601, 1:1000). Full scans of all immunoblotting is included in supplementary figure 9, including molecular weight markers.

Protein from conditioned media was obtained by plating 2.5 x 10^6 cells in media with 2% FCS for 16 hours before filtration through a 0.22 μm filter and then centrifugation at 4000g for 20minutes through a Vivaspin 6 concentrator column (10kDa molecular weight cut-off, GE healthcare). Coomassie staining of gels was performed as previously reported[50].

Hydrodynamic tail-vein injection

All animal experiments were approved by the German or UK legal authorities, and mice were kept under pathogen-free conditions in accordance with the institutional guidelines of the University of Tuebingen or University of Cambridge.

Male and female C57BL/6 mice were purchased from Charles River and injected at 5 – 8 weeks of age. Vectors for hydrodynamic injection were prepared with the Qiagen EndoFree MaxiPrep kit. Transposon-mediated gene transfer was previously described[8]; briefly 20µg of appropriate vector and 5µg of SB13 transposase-containing plasmid were diluted in sterile-filtered phosphate-buffered saline to a total volume of 10% of the body weight of the animal before being injected into the lateral tail vein in under 10 seconds.

Immunohistochemistry

Formalin fixed paraffin-embedded mouse tissues were stained with the following antibodies: anti-Notch1 (Cell signaling, 3608, 1:200); anti-Dec1 (a kind gift from Prof. Adrian Harris, 1:2000); anti-NRAS (Santa Cruz, sc-31, 1:100); anti-Hes1 (Cell signaling, 11988, 1:250); anti-p21 (BD, 556431); anti-CD3 (Dako, A0452, 1:1000); anti-B220 (R&D systems, MAB1217, 1:1500); anti-ki67 (Bethyl, IHC-00375, 1:1000); anti cleaved caspase 3 (Cell signaling, 9664, 1:1000) after heat-induced epitope retrieval in citrate (pH6) or Tris-EDTA (pH9) buffers before visualisation using the DAKO Envision kit according to manufacturers instructions and counterstaining with haematoxylin. Dual chromogenic IHC staining was performed on a Leica Bond Max (Leica) using the polymer refine detection and refine red detection

kits (Leica). For fluorescent labelling, we utilised anti-CD3 (as above) and anti-GFP (Abcam, ab13970, 1:100) with appropriate fluorochrome-tagged secondary antibodies (Life Technologies).

All slides were scanned on a Leica AT2 at 20x magnification and a resolution of 0.5µm/pixel. Following digitisation, image analysis was performed using the HALO (Indicalabs), utilising the Cytonuclear v1.4 algorithm. Each stain was trained independently to provide the best accuracy for cell counting and all the slides were reviewed manually following analysis to assess accuracy. NRAS staining was counted manually from 4 random high power fields containing a median of 1457 hepatocytes (range 1304 – 1678) as described previously [8], due to problems segmenting individual cells when staining was very intense.

Isolation and culture of human liver sinusoidal endothelial cells (HSEC)

Tissue samples and blood samples from patients were obtained with written informed consent and with local ethics committee approval (LREC reference 06/Q2702/61, Birmingham, UK and 04/Q2708/41, Birmingham, UK). Liver endothelial cells were isolated from explanted livers or donor tissue surplus to surgical requirements using a collagenase digestion (collagenase type 1a, Sigma-Aldrich) as described previously[60]. All tissue was collected from patients in the Liver Unit at Queen Elizabeth Hospital in Birmingham with informed consent and under local ethics committee approval. Briefly, digested tissue was placed over a 33% / 77% Percoll (Amersham Biosciences) density gradient. The endothelial cells were isolated by immunomagnetic selection using Abs against CD31 conjugated to Dynabeads (Life Technologies). The

endothelial cells were then cultured in medium composed of human endothelial basal growth medium (Life technologies), 10% AB human serum (HD supplies), 10ng/ml vascular endothelial growth factor (VEGF), and 10ng/ml hepatocyte growth factor (HGF) (Peprotech). The cells were grown in collagen-coated culture flasks and were maintained at 37^0C in a humidified incubator with 5% CO_2 until confluent.

Isolation of peripheral blood lymphocytes (PBLs)

PBLs were isolated as previously described[61] by density gradient centrifugation over Lympholyte (VH Bio) at 800xg for 25 minutes. Harvested Lymphocytes were re-suspended in RPMI 1640 (Life Technologies) /10% fetal calf serum.

Flow adhesion assay

To study immune cell recruitment, HSEC were grown in Ibidi µ-slide IV flow channels (Thistle scientific, Glasgow UK) until confluent. HSEC were then cultured in conditioned media for 24 hours prior to connection to the flow system previously described[35]. Peripheral blood lymphocytes were perfused through the microslides over the endothelial cells at a shear stress of 0.05Pa. Phase contrast video recordings made during lymphocyte perfusion were analysed offline to determine adherence.

Analysis of the *IL1A* locus

All sequence data was obtained from IMR90 cells. *IL1A* is shown with both the hg19 RefSeq annotation[62], and GenCode version 19 annotation[63].

C/EBPβ ChIP-Seq and DNAase-Seq data are from the Encode Project[39], and Histone data is from the Roadmap Epigenomics Project[40]. The data was visualised using the Gviz Bioconductor library.

Chromatin immunoprecipitation (ChIP)

ChIP was performed as described previously[64] with modifications. Briefly, 50ug of chromatin and 10ug of antibody (C/EBPβ: Santa Cruz sc-150) were applied to each IP. For the negative control no antibody was added to the IP. Three replicate ChIPs were carried out for each condition followed by qPCR. Primer sequences used in qPCR are as follows:

IL6 (-176/-122) F (target)*: GCCATGCTAAAGGACGTCACA

IL6 (-176/-122) R (target)*: GGGCTGATTGGAAACCTTATTAAGA

IL6 (-1158/-1094) F (non-specific)*: CCATCCTGAGGGAAGAGGG

IL6 (-1158/-1094) R (non-specific)*: CGTCGGCACCCAAGAATTT

IL8 (-134/-45) F (target)*: AAGTGTGATGACTCAGGTTTGC

IL8 (-134/-45) R (target)*: GCACCCTCATCTTTTCATTATG

IL8 (-1324/-1240) F (non-specific)*: TCACTGCTCTGTCGTACTTTCTG

IL8 (-1324/-1240) R (non-specific)*: CGCTTCTGGGCAAGTACATA

IL1A proximal F (target): CTGGCAGCTTAAGCCTGAGT

IL1A proximal R (target): TAAATTCCCCGTTTTGACGA

IL1A distal F (target): GGCCAGAGAACTGTGAGAGG

IL1A distal R (target): TGCATCAGGGCAAGTTTATG

IL1A non-specific F (non-specific): AGGGGCTAGATTTGGAGAGG

IL1A non-specific R (non-specific): ATTCACCCTGGAGCACAATC

* The primer sets for *IL6* and *IL8* were previously reported[6]. For IL1A 'Proximal' (promoter) and 'Distal' (enhancer), qPCR primers were designed based on C/EBPβ ChIP-seq data (ENCODE). In this case, 'non-specific' is upstream of the IL1A promoter. The locations of the primer sets for *IL1A* are illustrated in Supplemental Figure 8E.

Statistics and reproducibility.

No statistical method was used to predetermine sample size. The experiments were not randomised and the investigators were not blinded to allocation during experiments. Unless otherwise stated, data are represented by the mean ± SEM. *n* values represent the number of independent experiments performed or the number of individual mice per condition. For each independent *in vitro* experiment a minimum number of three experiments were performed to ensure reproducibility and adequate statistical power. For *in vivo* experiments all conclusions were based on a minimum of 3 mice per condition or time point. Analyses were conducted using Graphpad Prism 6. Student's *t*-test was used for two-condition comparisons; one-way ANOVA with Dunnett's multiple comparison test for more than 2 conditions. In the statistical analyses two-tailed tests were used throughout; a p-value of 0.05 was taken as significant. All the study data including statistical tests and exact p-values is provided in supplementary table 2.

Data availability

The RNA-Sequencing data generated for this study have been deposited at the Gene expression omnibus (GEO) with the accession numbers: GSE72404, GSE72407 and GSE72409. The mass spectrometry proteomics

data have been deposited to the ProteomeXchange Consortium via the PRIDE 82 partner repository with the dataset identifier PXD004168. (http://proteomecentral.proteomexchange.org).

The TGFB1 signature was derived from previously published data available from GEO under accession codes GSE12493[65] and GSE29660[66]. The CEBPB signature was derived from previously published data available from GEO under accession codes GSE47777 and GSE30834[37]. Chromatin immunoprecipitation datasets were obtained from GEO with the following accessions: CEBPB, GEO ID: GSM935519; DNase-Seq, GEO ID: GSM1008586; H3K27ac, GEO ID: GSM469966; H3K4me1, GEO ID: GSM521895; H3K4me3, GEO ID: GSM521901.

Proteomics data from Fig. 1 and Supplementary Fig. 1 have been provided as Supplementary Table 1. All other data supporting the findings of this study are available from the corresponding author on reasonable request.

SUPPLEMENTARY REFERENCES

49. Yagüe, E. *et al.* Ability to acquire drug resistance arises early during the tumorigenesis process. *Cancer Res.* **67,** 1130–1137 (2007).
50. Narita, M. *et al.* A Novel Role for High-Mobility Group A Proteins in Cellular Senescence and Heterochromatin Formation. *Cell* **126,** 503–514 (2006).
51. Aziz, N., Cherwinski, H. & McMahon, M. Complementation of defective colony-stimulating factor 1 receptor signaling and mitogenesis by Raf and v-Src. *Mol. Cell. Biol.* **19,** 1101–1115 (1999).
52. Capobianco, A. J., Zagouras, P., Blaumueller, C. M., Artavanis-Tsakonas, S. & Bishop, J. M. Neoplastic transformation by truncated alleles of human NOTCH1/TAN1 and NOTCH2. *Mol. Cell. Biol.* **17,** 6265–6273 (1997).
53. Cox, J. *et al.* A practical guide to the MaxQuant computational platform for SILAC-based quantitative proteomics. *Nat. Protoc.* **4,** 698–705 (2009).

54. Trapnell, C., Pachter, L. & Salzberg, S. L. TopHat: discovering splice junctions with RNA-Seq. *Bioinformatics* **25,** 1105–1111 (2009).
55. Anders, S. & Huber, W. Differential expression analysis for sequence count data. *Genome Biol.* **11,** R106 (2010).
56. Gonzalez, R. *et al.* Screening the mammalian extracellular proteome for regulators of embryonic human stem cell pluripotency. *Proceedings of the National Academy of Sciences* **107,** 3552–3557 (2010).
57. Sadaie, M. *et al.* Redistribution of the Lamin B1 genomic binding profile affects rearrangement of heterochromatic domains and SAHF formation during senescence. *Genes Dev.* **27,** 1800–1808 (2013).
58. Subramanian, A. *et al.* Gene set enrichment analysis: a knowledge-based approach for interpreting genome-wide expression profiles. *Proc. Natl Acad. Sci. U.S.A.* **102,** 15545–15550 (2005).
59. Livak, K. J. & Schmittgen, T. D. Analysis of relative gene expression data using real-time quantitative PCR and the 2(-Delta Delta C(T)) Method. *Methods* **25,** 402–408 (2001).
60. Shetty, S. *et al.* Common Lymphatic Endothelial and Vascular Endothelial Receptor-1 Mediates the Transmigration of Regulatory T Cells across Human Hepatic Sinusoidal Endothelium. *J. Immunol.* **186,** 4147–4155 (2011).
61. Lalor, P. F. *et al.* Vascular adhesion protein-1 mediates adhesion and transmigration of lymphocytes on human hepatic endothelial cells. *J. Immunol.* **169,** 983–992 (2002).
62. Pruitt, K. D. *et al.* RefSeq: an update on mammalian reference sequences. *Nucleic Acids Res.* **42,** D756–63 (2014).
63. Harrow, J. *et al.* GENCODE: the reference human genome annotation for The ENCODE Project. *Genome Res.* **22,** 1760–1774 (2012).
64. Schmidt, D. *et al.* ChIP-seq: using high-throughput sequencing to discover protein-DNA interactions. *Methods* **48,** 240–248 (2009).
65. Sargent, J. L. *et al.* A TGFbeta-responsive gene signature is associated with a subset of diffuse scleroderma with increased disease severity. *J. Invest. Dermatol.* **130,** 694–705 (2010).
66. Brennan, E. P. *et al.* Next-generation sequencing identifies TGF-β1-associated gene expression profiles in renal epithelial cells reiterated in human diabetic nephropathy. *Biochim. Biophys. Acta* **1822,** 589–599 (2012).

Figure 1_Narita

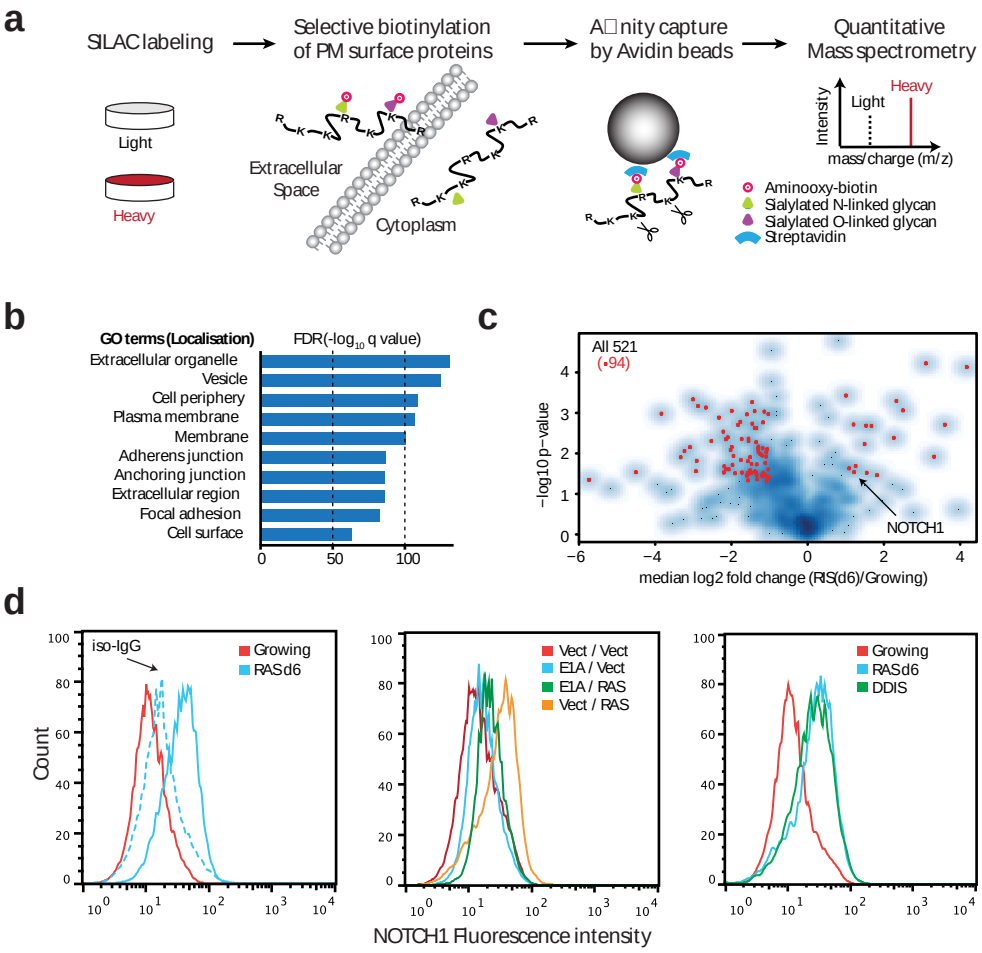

Figure 2_Narita

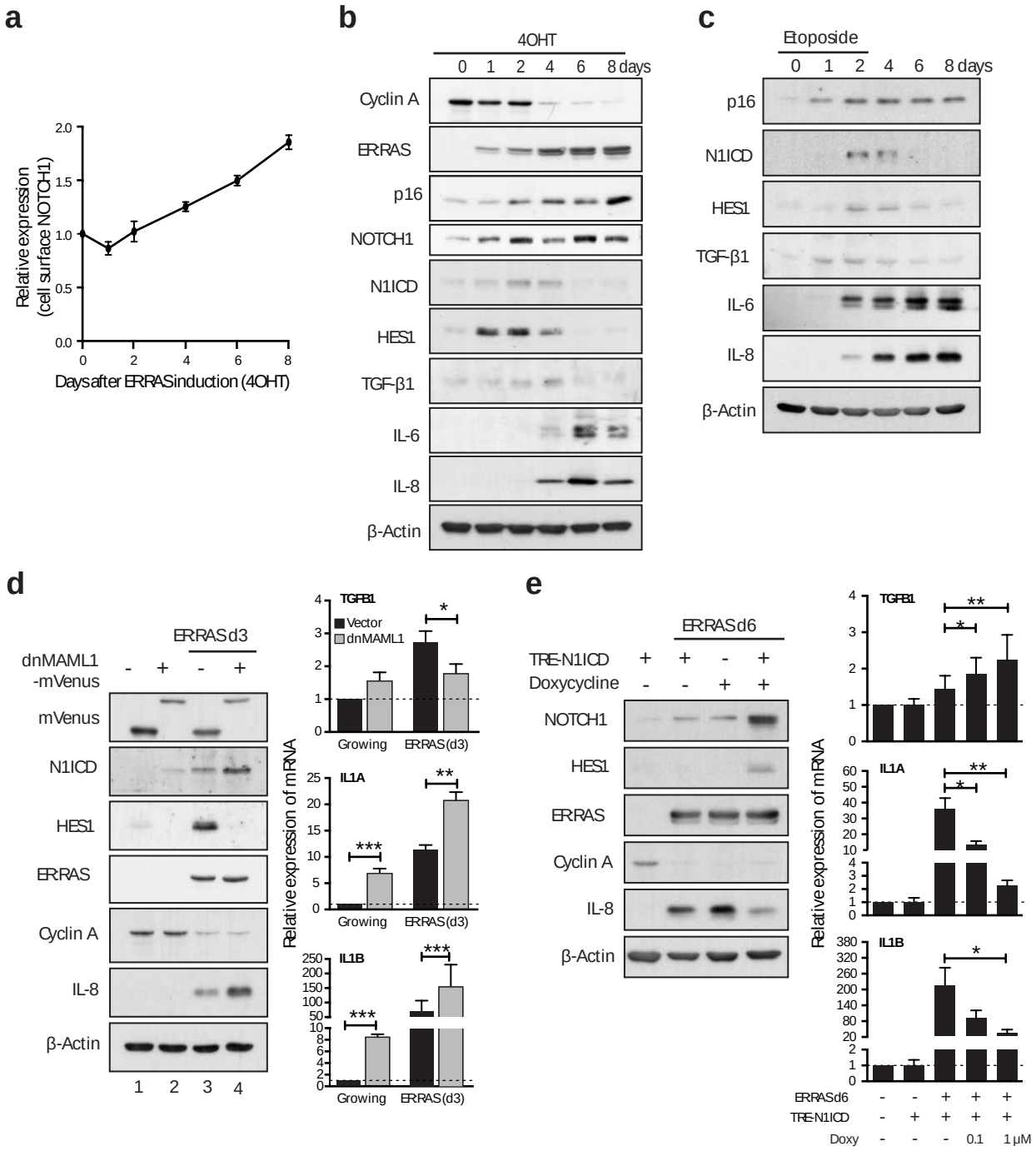

Figure 3_Narita

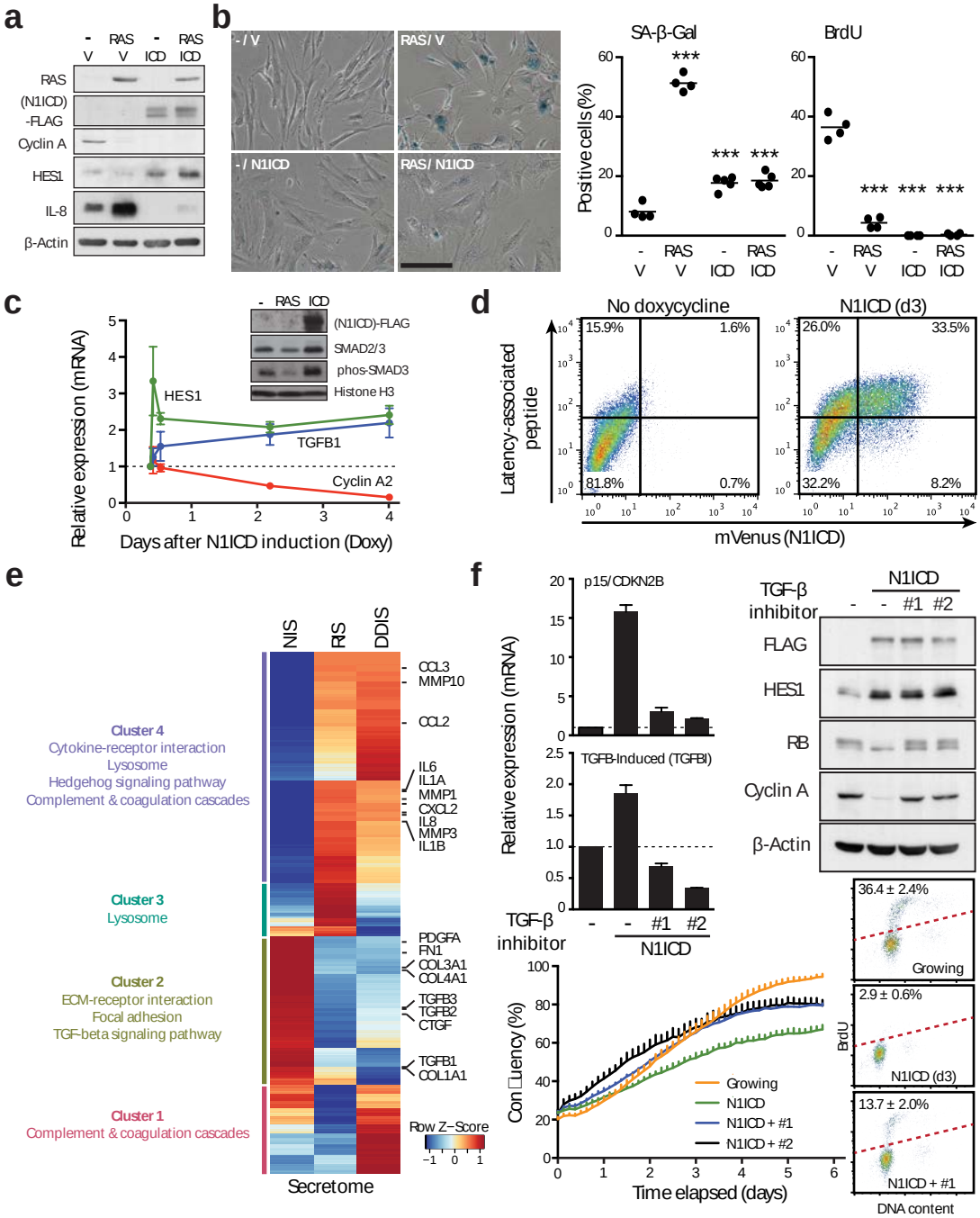

Figure 4_Narita

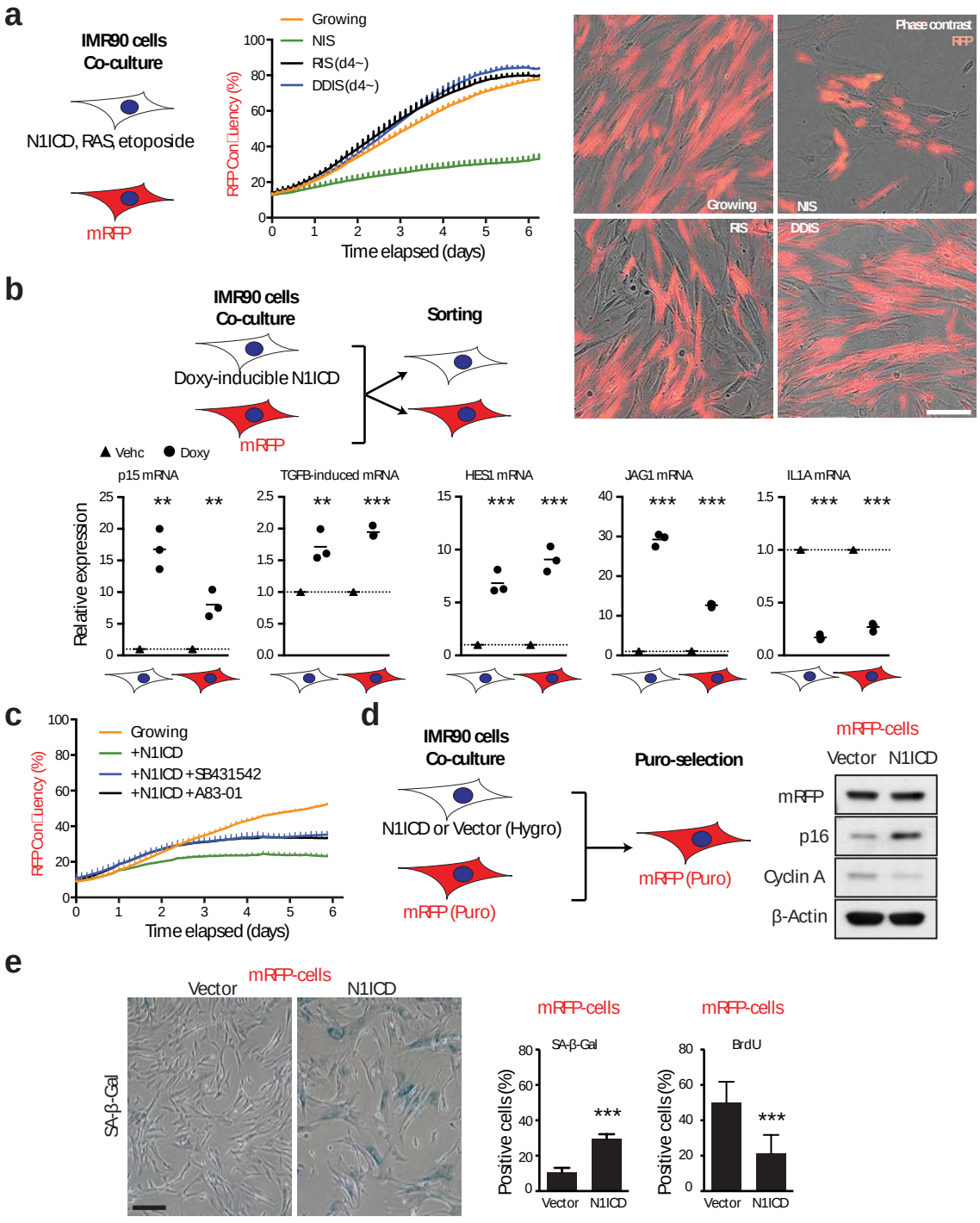

Figure 5_Narita

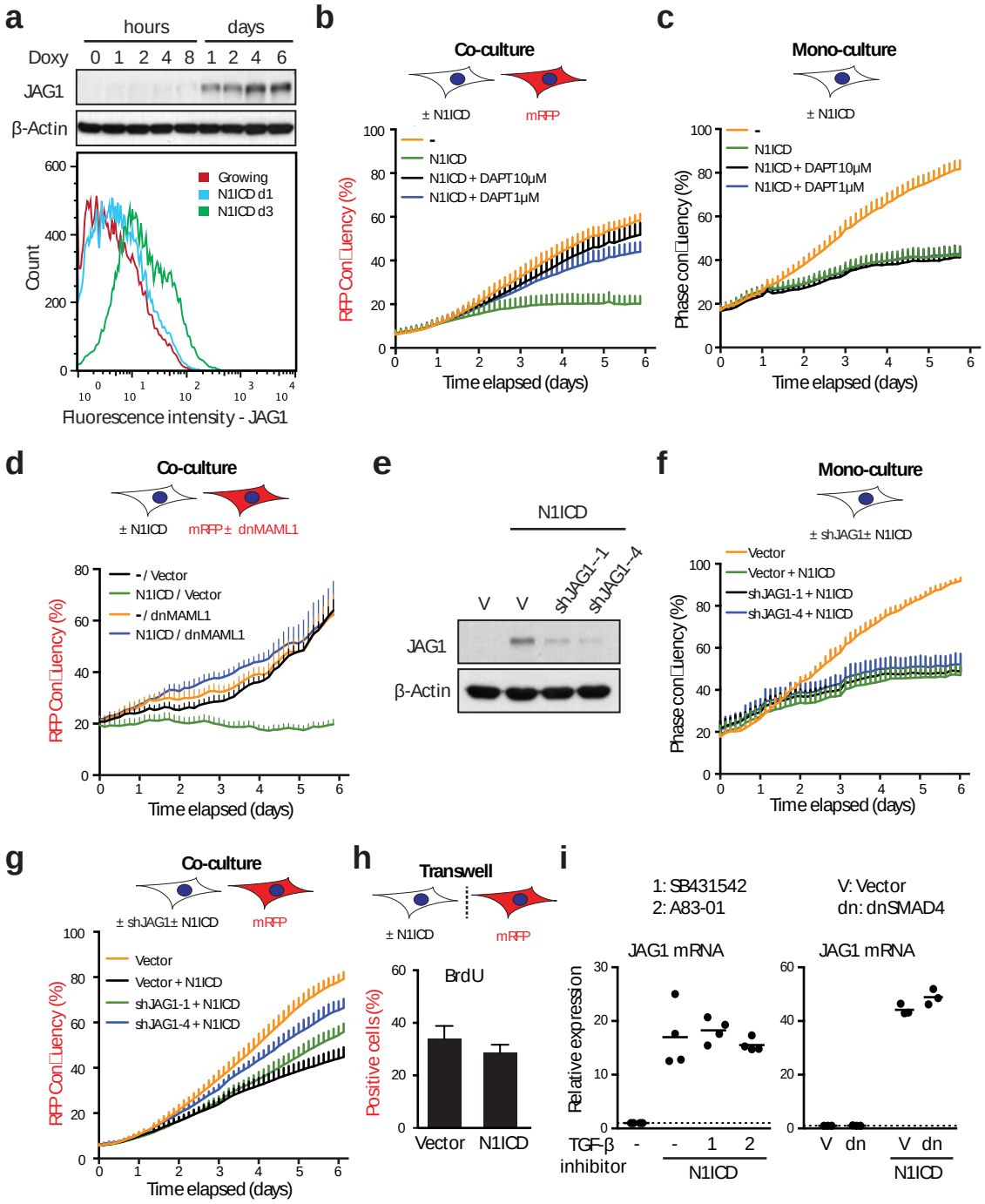

Figure 6_Narita

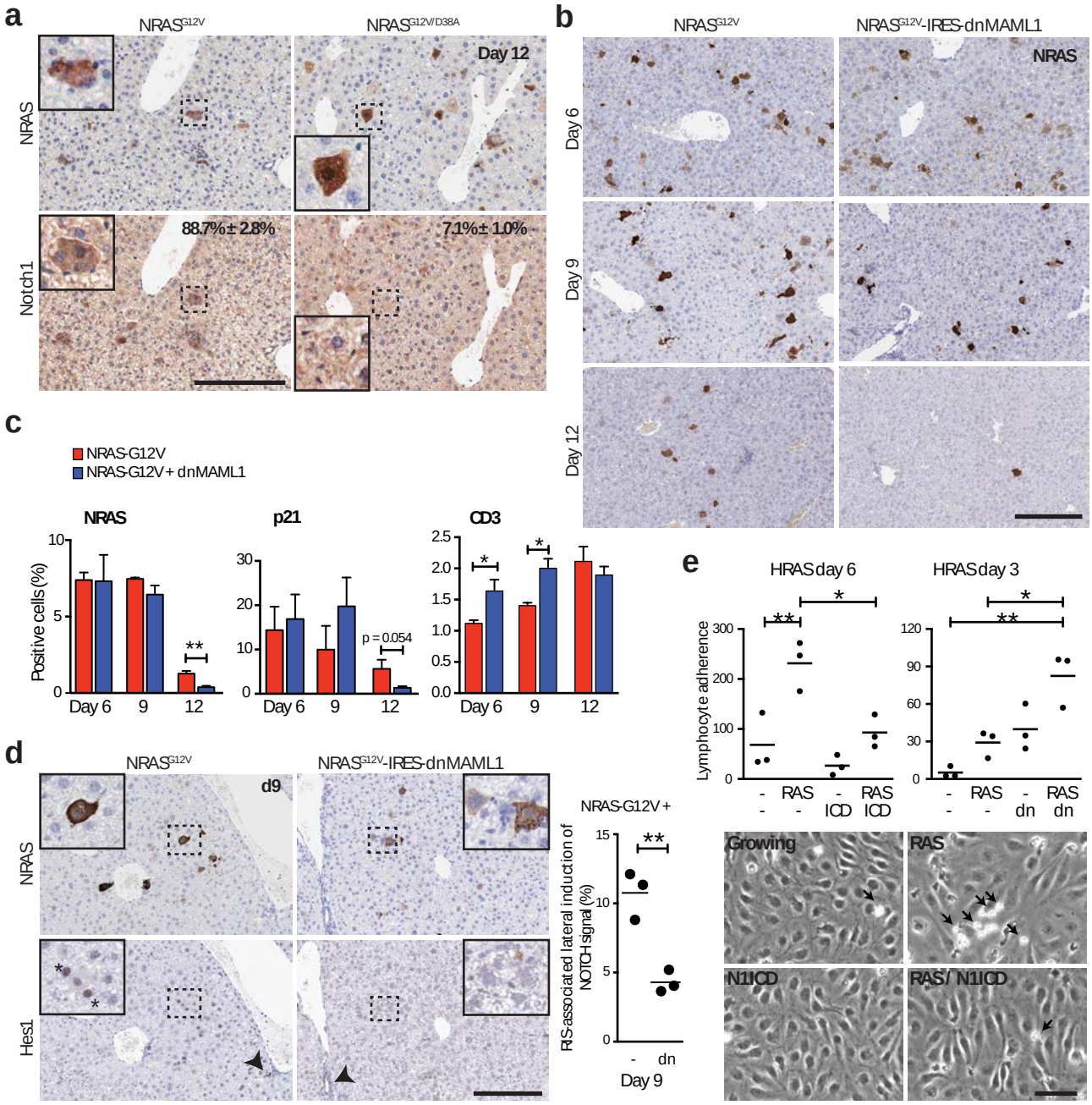

Figure 7_Narita

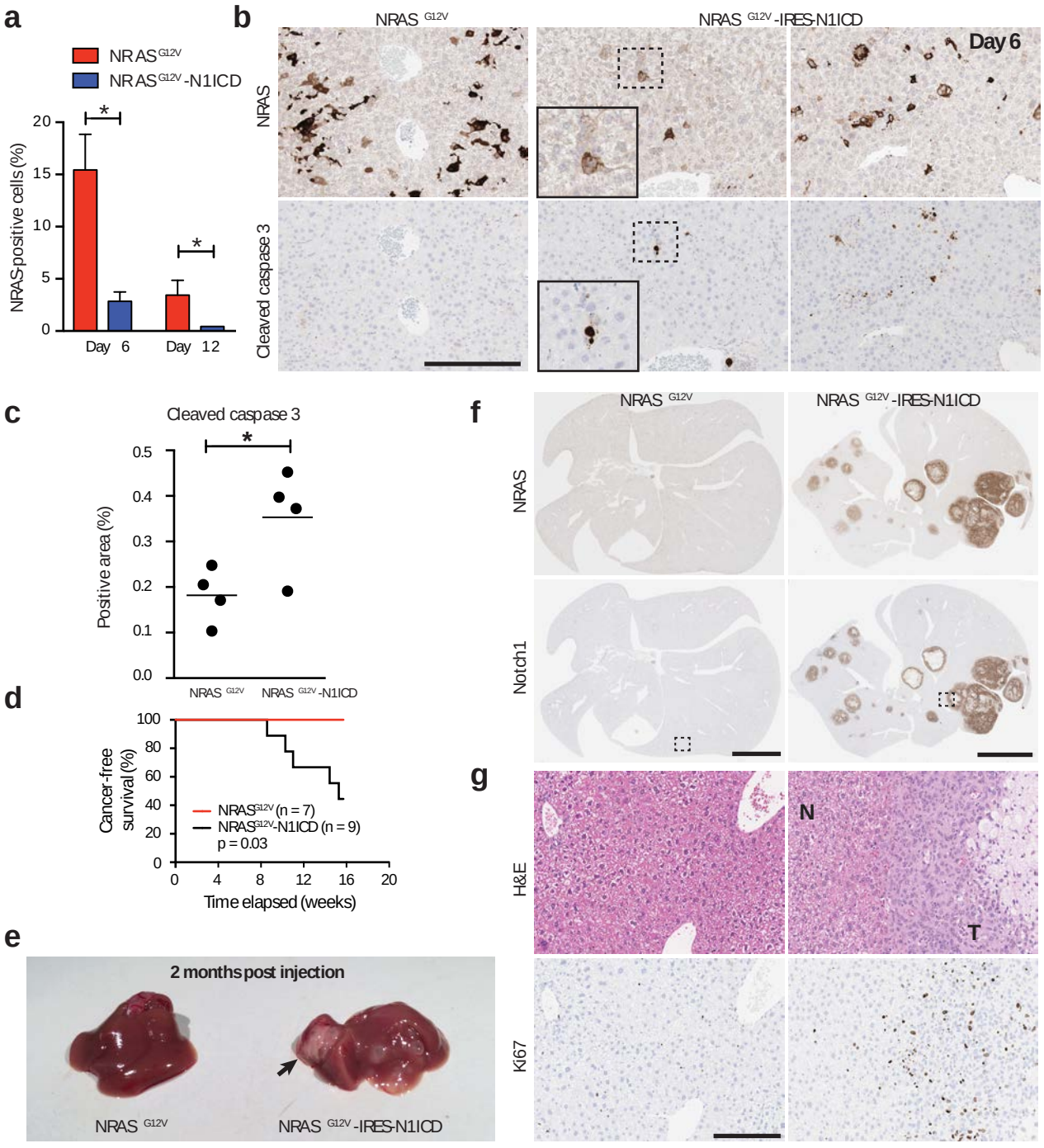

Figure 8_Narita